ICME impact at Earth with low and typical Mach number plasma characteristics

Antti Lakka[1], Tuija I. Pulkkinen[1,6], Andrew P. Dimmock[2], Emilia Kilpua[3], Matti Ala-Lahti[3], Ilja Honkonen[4], Minna Palmroth[3], and Osku Raukunen[5]

[1]Department of Electronics and Nanoengineering, Aalto University, Finland
[2]Swedish Institute of Space Physics, Uppsala, Sweden
[3]Department of Physics, University of Helsinki, Helsinki, Finland
[4]Finnish Meteorological Institute, Helsinki, Finland
[5]Department of Physics and Astronomy, University of Turku, Turku, Finland
[6]University of Michigan, Ann Arbor, USA

Correspondence: Antti Lakka (antti.lakka@aalto.fi)

Abstract.

We study how the the Earth's magnetosphere responds to the fluctuating solar wind conditions caused by interplanetary coronal mass ejection (ICME) events by using the Grand Unified Magnetosphere-Ionosphere Coupling Simulation (GUMICS-4). The two ICME events occurred on 15–16 July 2012 and 29–30 April 2014. During the 2012 event, the solar wind upstream values reached up to 35 particles/cm^3, speed of 694 km/s, and interplanetary magnetic field of 22 nT. The event of 2014 was a moderate one, with the corresponding upstream values of 30 particles/cm^3, 320 km/s and 10 nT. The mean upstream Alfvén Mach number was 2.3 for the 2012 event, while it was 5.8 for the 2014 event. We examine how the Earth's space environment dynamics evolves during both ICME events covering both global and local perspectives, including saturation of the cross-polar cap potential CPCP. To validate the accuracy of the GUMICS-4 simulation we use well-established references, such as the Shue model, and satellite data from different parts of the magnetosphere. We show that in the large scale, and during moderate driving, the GUMICS-4 results are in good agreement with the reference values. However, the local values, especially during high driving, show more variation. The CPCP saturation depends on one hand on the simulation resolution, and on the other hand on the Alfvén Mach number of the upstream solar wind.

1 Introduction

Present understanding is that the coupling of the solar wind and the Earth's magnetosphere occurs via magnetic reconnection (Dungey, 1961) and viscous processes (Axford and Hines, 1961) such as the Kelvin-Helmholtz instability (e.g. Nykyri and Otto (2001)) and diffusion (Johnson and Cheng, 1997). Although viscous processes may play a strong role, particularly when the interplanetary magnetic field (IMF) is northward (IMF $B_Z > 0$ nT) (e.g. Osmane et al. (2015)), magnetic reconnection on the dayside magnetopause is responsible for the majority of plasma transport across the magnetopause during southward interplanetary magnetic field IMF (IMF $B_Z < 0$ nT), allowing the solar wind to drive activity in the Earth's space environment (Nishida, 1968; Koustov et al., 2009). The intervals of extended periods of strongly southward IMF typically arise when the

Earth encounters an interplanetary coronal mass ejection (ICME) (see e.g. Kilpua et al. (2017b)). ICMEs are interplanetary counterparts of coronal mass ejections (CMEs), large eruptions of plasma and magnetic field from the Sun, driving the strongest geomagnetic disturbances (e.g., Gosling et al. (1991); Huttunen et al. (2002); Richardson and Cane (2012); Kilpua et al. (2017a)). The signatures of ICMEs at 1 AU include high helium abundance (Hirshberg et al., 1972), high magnetic field magnitude and low plasma beta (Hirshberg and Colburn, 1969; Burlaga et al., 1981), low ion temperatures (Gosling et al., 1973), and smooth rotation of the magnetic field (Burlaga et al., 1981). While there have been attempts to form a universal set of signatures to describe ICMEs (Gosling, 1990; Richardson and Cane, 2003), they vary significantly such that no single set of criteria are able to describe all the ICME events, and none of them are unique to ICMEs. For example, only one third to one half of all the ICMEs have a magnetic flux rope (or a magnetic cloud) (e.g. Gosling, 1990; Richardson and Cane, 2003), whose signatures combine enhanced magnetic field, reduced proton temperature, and the smooth rotation of the magnetic field over an interval of a day (Burlaga et al., 1981). While magnetic clouds are the most studied part of ICMEs due to their significant potential to cause large space storms, their relationship to the entire ICME sequence still pose many questions (e.g., Kilpua et al. (2013)). Moreover, if the ICME is sufficiently faster than the ambient solar wind plasma, a shock is formed ahead of the ICME (Goldstein et al., 1998), with a region of compressed solar wind plasma between the leading shock front and the magnetic cloud, referred to as the sheath region.

The sheath and ejecta are the most distinctive parts of ICMEs (see e.g. Kilpua et al. (2017b)), and both can drive intense magnetic storms (e.g. Tsurutani et al. (1988); Huttunen and Koskinen (2004)). However, they have clear differences in their solar wind conditions and consequently, their coupling to the magnetosphere is different (Jianpeng et al., 2010; Pulkkinen et al., 2007; Kilpua et al., 2017b). ICME sheaths typically include high solar wind dynamic pressure and fluctuating IMF, including both northward and southward orientations within a short time period (Kilpua et al., 2017b). The duration of the sheath is also typically shorter than the following cloud, for example Zhang et al. (2012) obtained the average values of 10.6 and 30.6 hours for sheaths and clouds, respectively. Sheaths are known to enhance high-latitude ionospheric currents (Huttunen and Koskinen, 2004), and they are found to have higher coupling efficiency than clouds (Yermolaev et al., 2012). The clouds typically enhance the equatorial ring current (Huttunen and Koskinen, 2004).

Due to potential for strongly southward IMF orientation, ICME magnetic clouds drive enhanced magnetospheric activity. Moreover, during cloud events, due to the combination of generally high magnetic fields and low plasma densities, the solar wind Alfvén Mach number M_A can reach quite low values and even be close to unity. The role of M_A for solar wind - magnetosphere coupling has been highlighted in recent studies (Lavraud and Borovsky, 2008; Lopez et al., 2010; Myllys et al., 2016, 2017). In particular, the role low M_A conditions typical to ICME magnetic cloud for the saturation of the ionospheric cross-polar cap potential CPCP has been a subject of several studies (e.g. Ridley, 2005, 2007; Lopez et al., 2010; Wilder et al., 2015; Myllys et al., 2016; Lakka et al., 2018).

Global MHD models have been used to study the effects of ICMEs on the magnetospheric and ionospheric dynamics. Wu et al. (2015) used the H3DMHD model (e.g. Wu et al., 2007) to examine a CME event on March 15, 2013. They found that the high-energy solar energetic proton time-intensity profile can be explained by the interaction of a CME-driven shock with the heliospheric current sheet embedded within nonuniform solar wind. A recent paper by Kubota et al. (2017) studied the Bastille

Day geomagnetic storm event (July 15, 2000) driven by a halo CME. They found that the inclusion of auroral conductivity in the ionospheric part of the global MHD model by Tanaka (1994) led to saturation of the CPCP without any effect on the field-aligned currents, thus suggesting a current system with a dynamo in the magnetosphere and a load in the ionosphere. The difficulty in assessing these studies is that they often do not include uncertainty estimate of the model results, while the methods are different for each study. Moreover, while the different MHD simulations are based on the same plasma theory, the approaches are different in terms of exact form of the equations, the numerical solutions, and the initial and boundary conditions, thus making comparisons of different models difficult. Nonetheless, understanding of the performance limits of the simulations is essential for meaningful comparisons to in-situ measurements.

Regardless of the different approaches used in gobal codes, the performance of the models have been assessed in several studies. Usually such assessments have been done through comparisons of the simulation results with in situ or remote observations of dynamic events or plasma processes (Birn et al., 2001; Pulkkinen et al., 2011; Honkonen et al., 2013). This is often not easy, as even small errors in the simulation configuration may create large differences with respect to the observations locally at a single point (Lakka et al., 2017), even if the simulation would reproduce the large-scale dynamic sequence correctly. Moreover, recent studies (Juusola et al., 2014; Gordeev et al., 2015) have shown that none of the codes emerges as clearly superior to the others, each having their strengths and weaknesses. In the absence of uniform code performance testing methodology, validating the results individually is important.

In this study we use the GUMICS-4 (Janhunen et al., 2012), global MHD simulation, and consider two ICME events, one having a significantly stronger solar wind driver than the other. To compare the two events, we use variables that are particularly sensitive to upstream changes, and examine how those variables are affected by the two events. The comparisons include the subsolar magnetopause position, the amount of energy transferred from the solar wind into the magnetosphere, the CPCP, and the magnetic field magnitude within the inner part of the magnetosphere, thus including both global and local variables. We especially focus on periods within the magnetic clouds within the ICMEs, by using two different spatial resolutions. We provide an uncertainty estimate (relative difference magnitude and standard deviation) for each quantity by comparing simulation results to well-established references, which include the Shue model (magnetopause location), the epsilon parameter (energy transferred through the magnetopause), the PCI index (CPCP), and in-situ measurements by Geotail and Cluster spacecraft (magnetic field magnitude).

This paper is structured in a following way: Section 2 describes GUMICS-4 global MHD code and the simulation setup, Section 3 describes characteristics of the two ICME events and the executed simulations, Section 4 presents the main results and Section 5 includes the discussion followed by conclusions.

2 Methodology

2.1 GUMICS-4 Global MHD Simulation

The simulations were executed using the fourth edition of the Grand-Unified Magnetosphere-Ionosphere Coupling Simulation (GUMICS-4), in which a 3D MHD magnetosphere is coupled with a spherical electrostatic ionosphere (Janhunen et al., 2012).

The finite volume MHD solver solves the ideal MHD equations with the separation of the magnetic field to a curl-free (dipole) component and divergent-free component created by currents external to the Earth ($\mathbf{B} = \mathbf{B_0} + \mathbf{B_1}(\mathrm{t})$) (Tanaka, 1994). The MHD simulation box has dimensions of 32 ... -224 $\mathrm{R_E}$ in X_{GSE} direcion and -64 ... +64 $\mathrm{R_E}$ in both Y_{GSE} and Z_{GSE} directions, while the inner boundary is spherical with a radius of 3.7 $\mathrm{R_E}$. GUMICS-4 uses temporal subcycling and adaptive cartesian octogrid to improve temporal and spatial resolution in key regions, which means that it only runs on a single processor due to difficulties in parallelizing computations with two adaptive grids. The temporal subcycling reduces the number of MHD computations an order of magnitude while maintaining the local Courant-Friedrichs-Levy (CFL) constraint (J.L. Lions, 2000, p. 121 — 151). The adaptive grid ensures that whenever there are large gradients, the grid is refined thus resolving smaller-scale features especially close to boundaries and current sheets.

The ionospheric grid is triangular and densest in the auroral oval, while in the polar caps the grid is still rather dense, with about 180 km and 360 km spacing used in the two regions, respectively. The ionosphere is driven by field-aligned currents and electron precipitation from the magnetosphere as well as by solar EUV ionisation. Field-aligned currents contribute to the cross-polar cap potential through

$$\nabla \cdot \mathbf{J} = \nabla \cdot [\Sigma \cdot (-\nabla\phi + V_n \times \mathbf{B})] = -j_{||} \left(\hat{\mathbf{b}} \cdot \hat{\mathbf{r}}\right), \tag{1}$$

where $\mathbf{J}$ is current density, Σ is the height-integrated conductivity tensor, ϕ is the ionospheric potential, V_n the neutral wind caused by the Earth's rotation, $j_{||}$ is the field-aligned current, and $\left(\hat{\mathbf{b}} \cdot \hat{\mathbf{r}}\right)$ is the cosine of the angle between the magnetic field direction $\hat{\mathbf{b}}$ and the radial direction $\hat{\mathbf{r}}$ (Janhunen et al., 2012). Electron precipitation and solar EUV ionisation have contributions on the height-integrated Pedersen and Hall conductivities with solar EUV ionisation parametrized by the 10.7 cm solar radio flux that has a numerical value of 100×10^{-22} $\mathrm{W/m^2}$. Electron precipitation affects the altitude-resolved ionospheric electron densities, and are used when computing the height-integrated Pedersen and Hall conductivities. The details on the ionsopheric part of GUMICS-4 can be found in Janhunen and Huuskonen (1993) and Janhunen (1996).

The region between the MHD magnetosphere and the electrostatic spherical ionosphere is a passive medium where no currents flow perpendicular to the magnetic field. The magnetosphere is coupled to the ionosphere using dipole mapping of the field-aligned current pattern and the electron precipitation from the magnetosphere to the ionosphere and the electric potential from the ionosphere to the magnetosphere. This feedback loop is updated every 4 seconds.

2.2 GUMICS simulations of two ICME events

We use both 0.5 and 0.25 $\mathrm{R_E}$ maximum spatial resolutions as well as varying dipole tilt angle in this study. Two complete ICME periods were simulated using 0.5 $\mathrm{R_E}$ resolution by starting with nominal solar wind conditions preceding the events, and ending with nominal conditions following the events. To give GUMICS-4 magnetosphere time to form (Lakka et al., 2017), the simulations were initialized with two hours of constant solar wind driving using upstream values equal to those during the first minute of the actual simulation ($n, |V|, |B|$ values of 4 $\mathrm{cm^{-3}}$, 310 $\mathrm{km/s}$ and 1.1 nT for the 2012 event, and 11 $\mathrm{cm^{-3}}$, 300 $\mathrm{km/s}$ and 1.8 nT for the 2014 event).

Due to computational limitations, using the best maximum spatial resolution (0.25 $\mathrm{R_E}$) covering both ICME events with full length is not feasible due to long simulation physical time (up to 3.5 days) and resulting long simulation running times. Hence, two additional runs were performed with 0.25 $\mathrm{R_E}$ maximum spatial resolution in order to gain a more detailed view of the dynamics of the magnetosphere and ionosphere when the ICME magnetic cloud was propagating past the Earth. These runs lasted 6 hours each, and were executed by restarting the 0.5 $\mathrm{R_E}$ runs with enhanced resolution. Table 1 summarizes all four simulation runs related to the study.

3 Observations of two ICME events

We use the solar wind data from the NASA OMNIWeb service (http://omniweb.gsfc.nasa.gov) and the solar energetic particle data from the NOAA NCEI Space Weather data access (https://www.ngdc.noaa.gov/stp/satellite/goes/index.html). Onset times for the ICME sheath (i.e., the shock time) and the magnetic cloud boundary times are retrieved from the Wind spacecraft ICME catalogue (https://wind.nasa.gov/ICMEindex.php). Figures 1 and 2 show the upstream parameters during both events. For both figures, IMF X, Y, Z components and the IMF magnitude are shown in panel a, upstream plasma flow velocity X, Y, Z components in panel b, the upstream plasma number density in panel c, upstream Alfvén Mach number (in logarithmic scale) in panel d, energetic proton fluxes for three GOES-15 energy channels between 8–80 MeV in panel e, and the cross-polar cap potential from the GUMICS-4 simulation in panel f. Figure 1 includes time range from 09:00 UT, July 14 to 15:00 UT, July 17, 2012, while Figure 2 shows the period from 19:00 UT, April 28 to 17:00 UT, May 1, 2014. The time of the ICME shock, and the start and end times of the ICME are marked with vertical red lines in both figures. The grey-shaded regions indicate the time periods simulated with the maximal 0.25 $\mathrm{R_E}$ spatial resolution. Both IMF and plasma flow velocity components are given in GSE coordinate system, which is also the coordinate system used by the GUMICS-4 simulation.

Figure 1 shows the arrival of the leading shock at 18:53 UT on July 14, 2012 as the simultaneous abrupt jump in the plasma and magnetic field parameters and the following ICME sheath as irregular directional changes of the IMF and compressed plasma and field. The energetic particle fluxes for the two lower energy channels increase until after the shock passage, which suggests continual particle acceleration in the shock driven by the ICME. At 06:54 UT on July 15, the onset of the ICME magnetic cloud is identified by strong southward turning of the IMF. Significant reduction in the number density, and the clear decrease in the variability of the interplanetary magnetic field. During the next 45 hours, the IMF direction stayed strongly southward while slowly rotating towards less southward orientation. We note that in the trailing part of the ICME, the field changes rather sharply to northward, thereafter continuing to rotate southward again. We cannot rule out that this end part is not another small ICME, but as our study focuses on the strong southward magnetic fields in the main part of the ICME we do not consider the origin of this end part further here.

The ICME on April 2014 was slower than the July 2012 ICME and its speed was very close to the ambient solar wind speed. Hence, no shock, nor clear sheath developed ahead of this ICME. The onset of the ICME-related disturbance is marked by the increased plasma number density followed by a rapid decrease and a clear southward turning of the IMF at 20.38 UT on April 29 (Figure 2). The weaker activity is also evident by the lack of energetic particle fluxes above background in the

magnetosphere. The very early phase of this cloud may contain some disturbed solar wind (the region of higher density and fluctuating field), but we do not identify it as a sheath and focus our study on the effects of the cloud proper.

Both magnetic clouds are characterized by low Alfvén Mach number. In the 2012 case, M_A drops even below unity and is 1.9 on average during the cloud structure, while during the 2014 magnetic cloud, the minimum M_A was 3.8 and the average was 5.8.

The 2012 event features generally larger CPCP, with values above 40 kV, and reaching 70 kV (Figure 1f). On the other hand, during the 2014 event the CPCP peaks early at 50 kV and subsequently reduces to 20 kV (Figure 2f).

The 2012 ICME event is considerably longer than the 2014 event, with 57h 26min total duration, of which 12h 1min are sheath, and 45h 25min part of the magnetic cloud passage. The 2014 event lasted 21 h 13 min in total. The 2012 ICME had larger effects on magnetospheric activity, as the solar wind driving was considerably stronger, with the average IMF magnitude and solar wind speed of 14 nT and 490 $\mathrm{km/s}$, respectively, compared with 8.5 nT and 303 $\mathrm{km/s}$ of the 2014 event. The maximum IMF magnitude and upstream solar wind speed were also larger during the 2012 event, with 21 (10) nT and 660 (321) $\mathrm{km/s}$ maximum values measured during the 2012 (2014) cloud. However, while maximum number density was higher during the 2012 magnetic cloud (36 $\mathrm{cm^{-3}}$ vs. 30 $\mathrm{cm^{-3}}$), the average number density was considerably higher during the 2014 event (2012: 2 $\mathrm{cm^{-3}}$ vs. 2014: 12 $\mathrm{cm^{-3}}$).

During the two ICME events, data from the Cluster 1 (hereafter Cluster) and Geotail satellites were available from the CDAWeb service (https://cdaweb.sci.gsfc.nasa.gov/index.html/). Figure 3 shows the orbits of Cluster (blue) and Geotail (green) along with the magnetopause location (black) from the empirical Shue model (Shue et al., 1997) on the XY plane (figures 3a and 3c) and on the XZ plane (figures 3b and 3d) for both events. The magnetopause position is computed for the most earthward magnetopause location during the events, while the orbit tracks include intervals of nominal upstream conditions before and after the ICME events. Start and end points of the time intervals are marked with a cross and a triangle, respectively. Dots mark the points where satellite orbits intersect (located visually) the innermost position of the magnetopause. The variability of the magnetopause position means that between those orbit tracks the S/C may cross to outside the magnetosphere. The used coordinate system is GSE. Based on figure 3, the Cluster spacecraft orbits inside of the magnetosphere throughout the 2012 event and for most of the 2014 event. On the other hand, Geotail is outside the magnetosphere an extended period during July 16-17, 2012 as well as during several periods in April–May 2014.

Figures 4 and 5 show time series of the magnetic field magnitude $|B|$ along the Geotail (panel a) and Cluster (panel b) orbits during the 2012 and 2014 events. Green (Geotail) and blue (Cluster) curves show the observations, while the black (magenta) curve shows the magnetic field magnitude along the spacecraft orbits in GUMICS-4 simulation using 0.5 (0.25) $\mathrm{R_E}$ maximum spatial resolution. The yellow-shaded regions in panels a and b indicate times when the spacecraft may encounter magnetopause crossings. Note that a logarithmic scale is used for the Cluster data. Panel c in both figures shows the radial distance of the spacecraft from the center of the Earth. Note that satellite measurements have been interpolated over long (several hours) datagaps, most notably on July 16, 12:15–18:45 UT.

At the start of the 2012 event, Geotail resides in the plasma sheet, but quickly moves to the boundary layer (roughly July 14, 16:00 UT to July 15, 06:00 UT), after which it enters the lobe as the cloud proper hits the magnetosphere. At around the end

of the data gap at the end of July 16, the spacecraft moves to the low latitude boundary layer and the magnetosheath (identified from plasma data not shown here).

At the start of the 2012 event, Cluster is near perigee recording field values dominated by the dipole contribution. Cluster exits the ring current region around 16:00 UT on July 14, and enters the plasma sheet. A brief encounter in the lobe is recorded between roughly 18:00 UT July 15 and 06:00 July 16. A second period in the inner magnetosphere commences around 12:00 UT on July 16, with exit to the lobe after 00:00 UT July 17 (identified from plasma and energetic particle data not shown here).

4 Analysis

4.1 Global dynamics

Figures 6 and 7 show the effect of upstream IMF B_Z (panel a), and solar wind dynamic pressure (panel b) on the magnetopause nose (panel c), total energy through the dayside magnetopause nose position (panel d) and the ionospheric cross-polar cap potential CPCP (panel e) during the simulated intervals shown in figures 1 and 2. The 0.5 $\mathrm{R_E}$ resolution run results are shown in black, and 0.25 $\mathrm{R_E}$ resolution results are shown in magenta. Grey shaded area highlights the 6-hour interval simulated using both resolutions. Blue and green curves indicate reference values (see below) and solar wind upstream conditions, respectively. As a metrics for validating the simulation results, we use the magnitude of the relative difference (given as δ in panels c, d and e of figures 6 and 7)

$$\delta = \left| \frac{x_{\mathrm{ref}} - x_{\mathrm{GUMICS-4}}}{x_{\mathrm{ref}}} \right|, \tag{2}$$

in which x is the GUMICS-4 variable and x_{ref} refers to the reference parameter value of the variable. An average δ value is computed for each ICME simulation phase (nominal solar wind, sheath, cloud) for both 0.5 $\mathrm{R_E}$ and 0.25 $\mathrm{R_E}$ resolution runs. These percentage values can be found in tables 2 and 3. We also compute standard deviation (SD) for the reference vs. GUMICS-4 results. A single SD value (given in panels c, d and e) is computed for the 0.5 $\mathrm{R_E}$ resolution runs to illustrate how similar the temporal evolution is over time scales of days for GUMICS-4 and the reference parameter.

Figures 6a and 6b show that the IMF B_Z fluctuates approximately between -5...+5 nT during nominal solar wind conditions, while the solar wind dynamic pressure is steady and low. At the onset of ICME sheath, both B_Z and dynamic pressure start fluctuating with increased amplitude. Moreover, after the onset of ICME cloud, the orientation of the IMF slowly rotates from southward to northward with the solar wind dynamic pressure decreasing rapidly and remaining low until the end of the simulated interval. This behaviour is somewhat similar during the 2014 event (figures 7a–7b), with the exception of missing high amplitude fluctuations due to absence of a distinct ICME sheath.

In GUMICS-4, we identify the magnetopause nose position as a single grid point having the maximum value of J_Y along the Sun-Earth line, using one-minute temporal resolution, smoothed using 10-min sliding averages. This value is compared with the Shue (Shue et al., 1997) empirical magnetopause model. For simplicity, the nose of the magnetopause is referred to a magnetopause. Figure 6c shows that at the onset of ICME sheath, the magnetopause moves Earthward as a consequence of changing upstream conditions, which is followed by Sunward return motion lasting until the end of the ICME event. The

average δ is highest during the cloud (8%) and lowest (2.5%) during nominal solar wind conditions. During ICME sheath, average δ is 4.5%. During the 2014 event, the magnetopause starts moving Earthward at least 10 hours before the onset of ICME cloud (figure 7c), as the dynamic pressure increases, with IMF B_Z staying positive. After the onset however, the magnetopause moves Sunward for a few hours until slowly moving Earthward again. The difference in average δ between cloud and nominal solar wind conditions is lower than for the 2012 event, as the respective values are 3.3% and 2.4%.

The grey-shaded region in figure 6c shows that during the first four hours of the 6-hour run the magnetopause position predictions (black and magenta curves) by GUMICS-4 are within 5% of the Shue et al. (1997) model (blue curve). During the last 2 hours, however, there are more fluctuations in the GUMICS-4 magnetopause position, especially in the 0.5 $\mathrm{R_E}$ resolution run. From July 15, 21:00 UT to July 16, 01:00 UT the simulation runs agree on the magnetopause location and also with the Shue model, with differences within 10% all the time of the first 4 hours. However, the last two hours show more variations between the three curves: The finest resolution show slight outward motion of the magnetopause, which toward the end of the period is less than that predicted by the Shue model. On the other hand, the 0.5 $\mathrm{R_E}$ resolution run shows inward indentations followed by outward motion consistent with the Shue model. Overall, the 0.5 $\mathrm{R_E}$ resolution run is 58% of the time within 10% of the Shue model, and the 0.25 $\mathrm{R_E}$ resolution run agree 67% of the time within 10% of the Shue model. Despite the fact that average relative difference is slightly lower for the 0.5 $\mathrm{R_E}$ resolution run (4.9%) than for the 0.25 $\mathrm{R_E}$ resolution run (5.6%), over the entire 6-hour periods, the 0.25 $\mathrm{R_E}$ run is within 10% of the Shue model 92% of the time, while the 0.5 $\mathrm{R_E}$ run reaches within 10% 89% of the time due to the 0.5 $\mathrm{R_E}$ run being more inclined toward moving more Earthward during the last two hours of the 6-hour period.

The time evolution of the magnetopause position during the 6-hour period in Figure 7 is similar for both spatial resolutions, with both simulation runs responding similarly to small upstream fluctuations. Both simulation runs stay within 10% of the Shue model prediction for the entire 6-hour period. Average relative difference is only slightly lower for the higher resolution run (3.2%), than for the lower resolution run (4.5%).

Overall, the higher-resolution run yielded better agreement with the magnetopause location especially for a moving magnetopause nose (2012 event), because increasing the spatial resolution sharpens the gradients and allows better identification of the location of the maxima (Janhunen et al., 2012). Comparison of the runs shows, however, that the results are consistent with each other, indicating that the lower-resolution run is providing similar large-scale dynamics as the finer-resolution run. Furthermore, increased δ during the 2012 ICME cloud and overall higher δ during the 2012 event indicate that GUMICS-4 accuracy in the magnetopause nose position prediction is better during weaker solar wind driving. This is further demonstrated by the standard deviation values, which are 0.661 for the 2012 event, and 0.321 for the 2014 event (see figures 6c and 7c).

Total energy through the dayside magnetopause is computed by evaluating the energy flux incident at the (Shue) magnetopause, and it is evaluated from

$$\mathbf{K} = \left(u + p - \frac{B^2}{2\mu_0}\right)\mathbf{V} + \frac{1}{\mu_0}\mathbf{E}\times\mathbf{B}, \tag{3}$$

where u is the total energy density, p pressure, B magnetic field, $\mathbf{V}$ flow velocity and $\mathbf{E}\times\mathbf{B}$ the Poynting flux, and its component perpendicular to the magnetopause surface. As is shown in figure 6c, the relative difference magnitude δ in the

magnetopause nose location can reach up to 30% values. To avoid underestimating the size of the magnetosphere, we evaluate the magnetopause surface by moving the radial distance of each Shue magnetopause surface value 30% further away from the Earth. This surface is then used in integrating the energy flux values entering the magnetosphere Sunward of the terminator ($X > 0$ $\mathrm{R_E}$). The results are shown for the 2012 event in figure 6d for both 0.5 and 0.25 $\mathrm{R_E}$ resolution runs along with the computed ϵ-parameter (Perreault and Akasofu, 1978):

$$\epsilon = \frac{4\pi}{\mu_0} V B^2 \sin^4(\frac{\theta}{2}) l_0^2, \tag{4}$$

where μ_0 is vacuum permeability, B and V are the magnitudes of the IMF and solar wind plasma flow velocity, θ is the IMF clock angle, and l_0 is an empirically determined scale length.

While both resolution runs agree with each other, it is evident that their numerical values are quite far from the reference, ϵ-parameter. It should be noted however, that the ϵ-parameter is not scaled to represent the energy input, but the energy dissipated in the inner magnetosphere (Akasofu, 1981). Thus the relative difference is not a good metrics to describe the difference between GUMICS-4 and the ϵ-parameter. However, general temporal evolution is similar for most parts of ICME cloud, with both GUMICS-4 and the ϵ-parameter reproducing steep increase at the onset of cloud as well as subsequent slow decrease, as is shown by the computed SD value in figure 6d (2.263). As in the case of the 2012 event, the two simulation runs using different spatial resolutions are almost inseparable in terms of the incoming solar wind energy during the 2014 event (Figure 7d). During moderate solar wind driving in 2014, GUMICS-4 is closer to the ϵ-parameter, with considerably lower SD value (0.725) compared with the 2012 event. This is an interesting characteristics of the ϵ-parameter warranting further study.

Differences between the simulations executed using different spatial resolutions in local measures, such as the magnetopause nose position, do not show in global variables, such as the total energy through the dayside magnetopause surface. As can be seen in Figure 6d, the curves of the two different spatial resolution runs are almost identical. This emphasizes that integrated quantities, such as energy, give a better representation of the true physical properties of the magnetosphere in the GUMICS-4 solution and are not dependent on grid resolution (Janhunen et al., 2012). We acknowledge that using more sophisticated methods for identifying the magnetopause surface from the simulation could potentially lead to some changes in the results. The Shue model was used for its simplicity and computational ease. Our results agree in general with Palmroth et al. (2003) who identified the magnetopause by using plasma flow streamlines from GUMICS-4, indicating that the use of the Shue model is not introducing large errors in the energy estimates.

The magnetosphere – ionosphere coupling, here illustrated by the CPCP time evolution in Figure 6e, is compared with the polar cap index (Ridley and Kihn, 2004) computed as

$$PCI = 29.28 - 3.31 sin(T + 1.49) + 17.81 PCN, \tag{5}$$

where T is month of the year normalized to 2π, and PCN is the nothern polar cap index retrieved from OMNIWeb. The PCI is a very indirect proxy (based on a single-point measurement only) for the CPCP, and thus the comparisons must be interpreted with great care. It is worth noting, that for the 2012 event, GUMICS-4 is closest to PCI in terms of δ during the ICME cloud, with 36.0% average difference between the two. The difference is larger during nominal solar wind conditions and ICME sheath phase, with average δ values of 64.9% and 57.6%.

The 0.25 $\mathrm{R_E}$ and the 0.5 $\mathrm{R_E}$ runs differ from each other in terms of the polar cap potentials. For the 2012 event, the higher resolution run produces 20-30% higher CPCP than the lower resolution run during the first three hours of the 6-hour phase. During the last 3 hours, the CPCP predicted by the 0.5 $\mathrm{R_E}$ run increases significantly to almost reach the high-resolution run cross-polar cap potential. This coincides with the time when the magnetopause moves further away from the Earth. On average the difference to PCI index is 31.2% (0.5 $\mathrm{R_E}$ run) and 16.3% (0.25 $\mathrm{R_E}$ run) during the 6-hour period simulated using both resolutions.

Figure 7e shows that the relative difference between the PCI index and GUMICS-4 is greatest during ICME cloud (69.2% on average) compared with 46.9% average difference during nominal solar wind conditions. However, while the 2012 and 2014 events are similar in terms of higher CPCP in the fine resolution simulation (up to 250% in the 2014 event), CPCP is quite stable during the 2014 event in both low and high resolution throughout the 6 hour interval. As in the case of the 2012 event, the higher resolution run is closer to the PCI index, with average relative difference resulting as 70.0% and 27.0% for the 0.5 and 0.25 $\mathrm{R_E}$ resolution runs respectively during the 6-hour phase.

In terms of the SD values, GUMICS-4 and the PCI index show better agreement in the temporal evolution of CPCP during the 2014 event (SD = 15.838) than during the 2014 event (SD = 5.107). However, these SD values are clearly highest of all three (magnetopause nose, energy, CPCP) for both events. This is in part due to the ionospheric (local) processes contributing to the PCI index but not related to the large-scale potential evolution.

4.2 Saturation of the Cross-polar cap Potential

Figures 8 and 9 show the CPCP (both northern and southern hemispheres) as a function of the solar wind electric field E_Y component for both ICME events. Color-coding marks the IMF magnitude in figures 8a and 9a, solar wind speed in figures 8b and 9b, and the upstream Alfvén Mach number in figures 8c and 9c. Every data point in Figure 8 (9) is computed from 10-minute averages, binned by E_Y with 1.0 (0.5) $\mathrm{mV/m}$ intervals. The ICME sheath (solid circles) and cloud (solid squares) periods as well as the nominal solar wind conditions (solid triangles) prior to and following the events are analyzed separately. Note that here only the coarse grid (0.5 $\mathrm{R_E}$) simulation results are used, as we analyze the effects during the entire magnetic cloud and sheath periods including times before and after the event not covered by the high-resolution run.

Figure 8 shows that the response of the CPCP to the upstream E_Y is quite linear during the magnetic cloud (squares) when solar wind driving electric field E_Y is below 5 $\mathrm{mV/m}$, during nominal solar wind conditions (triangles), and ICME sheath (diamonds). However, the polar cap potential first decreases and subsequently saturates during the cloud when the solar wind driving is stronger ($E_Y > 5$ $\mathrm{mV/m}$). For the 2012 event, we refer to the E_Y range from 0 to 5 $\mathrm{mV/m}$ as the linear regime, and from 5 $\mathrm{mV/m}$ upward as the non-linear regime.

Figure 8a shows the obvious result that highest E_Y values are associated with highest IMF magnitudes. However, it also shows that the largest IMF magnitudes are associated with the non-linear regime, indicating that strong upstream driving leads to CPCP saturation. In addition, Figure 8b suggests that the increase of the CPCP in the linear regime is clearly higher for lower velocity values (cloud structure), than for higher velocity values (sheath and nominal conditions). Generally, this agrees with the previous studies utilizing statistical (Newell et al., 2008) and numerical (Lopez et al., 2010) tools. The latter authors suggest

that this is caused by the solar wind flow diversion in the pressure gradient-dominated magnetosheath; faster solar wind will produce more rapid diversion of the flow around the magnetosphere, and thus smaller amount of plasma will reach the magnetic reconnection site.

Figure 8c shows that the upstream Alfvén Mach number M_A is at or above 4 ($M_A \geq 4$) during the nominal solar wind conditions and during the ICME sheath, while during the magnetic cloud M_A resided below 4 and almost reaches unity. This supports the interpretation that saturation of the CPCP depends on the upstream Alfvén Mach number M_A such that saturation occurs only when M_A values fall below 4. The dependence of the CPCP saturation on M_A is well-known, documented both in measurements (Wilder et al., 2011; Myllys et al., 2016) and in simulation studies (Lopez et al., 2010; Lakka et al., 2018).

Figure 9 agrees with the view presented above, as the response of the CPCP to the upstream E_Y during the 2014 event is quite linear regardless of the IMF magnitude (Figure 9a), plasma flow speed (Figure 9b), or the large-scale solar wind driving structure (ICME cloud or nominal solar wind). This is apparently because solar wind driving is substantially weaker during the 2014 event than during the 2012 event, with the IMF magnitude reaching barely 10 nT, and upstream plasma flow speed varying only of the order of 10 $\mathrm{km/s}$. As a result, the upstream Alfvén Mach number $M_A > 4$ throughout the ICME event as well as during the nominal solar wind conditions. The high polar cap potential values for the lowest E_Y bin is associated with the large density enhancement driving polar cap potential increase before the arrival of the cloud proper.

Figure 10 shows the region 1 and region 2 field-aligned current (FAC) system coupling the magnetosphere and the ionosphere (e.g. Siscoe et al. (1991)). The four panels show how field-aligned currents are distributed in the northern hemisphere ionosphere in July 16, 2012 at 01:00 UT and 03:00 UT at 0.5 $\mathrm{R_E}$ maximum resolution (figures 10a–10b) and at 0.25 $\mathrm{R_E}$ maximum resolution (figures 10c–10d). Current density is shown both as color coding and contours, while the white dotted line depicts the polar cap boundary. The distribution of the FAC do not change much in either of the simulations, thus suggesting that the coupling of the magnetosphere and the ionosphere remains relatively constant. However, as is shown in figure 6e, the CPCP shows different temporal evolution based on the used spatial resolution, with increasing (constant) CPCP in the 0.5 (0.25) $\mathrm{R_E}$ simulation, thus suggesting that while the magnetosphere - ionosphere coupling is unaffected, the solar wind - ionosphere coupling is affected of enhanced spatial resolution.

4.3 Local dynamics

Figures 4 and 5 show the time series of the IMF magnitude $|B|$ in the Geotail and Cluster orbits during the 2012 and 2014 events compared with the GUMICS-4 results along the satellite tracks. The relative difference magnitude in $|B|$ between GUMICS-4 and both satellites as well as standard deviations are computed using the same methods as in section 4.1, and are given in panels a and b. Since the inner boundary of the GUMICS-4 MHD region is at 3.7 $\mathrm{R_E}$, the times when Cluster is closer than 3.7 $\mathrm{R_E}$ to Earth are ignored when computing δ and SD values.

Prior to the arrival of the sheath region in 2012, Geotail enters the plasma sheet boundary layer earlier than predicted by GUMICS-4. During the ICME sheath there are many dips and peaks in both plots, with the difference between measured (both Geotail and Cluster) and predicted values varying, as can be seen from figures 4a and 4b. Also, Figure 4a shows that starting from July 17, 06:00 UT the measured field at Geotail increases as the satellite goes to the magnetosheath proper, while

GUMICS-4 prediction decreases as the orbit track in GUMICS-4 approaches the shock region (see Figure 3a). The 2014 event shows similar features especially when Geotail enters and exits the magnetosphere at 23:14 UT, April 28, and at 12:00 UT, April 30, respectively, with measured (by Geotail) $|B|$ in the former case fluctuating and rising sharply from 10 nT to 40 nT while the GUMICS-4 $|B|$ increases more steadily from a few nT to 20 nT as the satellite enters from the magnetosheath to the magnetosphere. In the latter case decrease (increase) of measured (simulated) $|B|$ occurs several hours after the spacecraft exits the magnetosphere (later yellow-shaded region in Figure 5a) because of the differences in the moment of exit (and exact location of the magnetopause location). Note that while Cluster makes an entry into the magnetosphere at 16:12 UT, April 29, GUMICS-4 predicts a position within the magnetosheath and an entry into the magnetosphere only following the end of the cloud.

Note that the Cluster perigee (2 $\mathrm{R_E}$) (Figure 4c) is below the inner boundary of the GUMICS-4 simulation (3.7 $\mathrm{R_E}$), which causes the simulation field to record unphysical values around the time of the maxima at 09:00 on July 14, 2012 and 15:00 on July 16, 2012, hence the data gaps in GUMICS-4 data plots.

The effect of the ICME sheath is visible after its arrival in Figure 4, with both measured and predicted $|B|$ fluctuating. The ICME magnetic cloud proper seems to cause largest difference in $|B|$ during the 2012 event, when the driving was quite strong. Tables 4 and 5 summarize average δ over each ICME phase (nominal solar wind conditions, sheath, cloud). Moreover, average δ is given also over times when the spacecraft is located inside and outside the magnetosphere. The relative difference magnitude in $|B|$ between GUMICS-4 and in-situ measurements ranges between 34.4% and 79.7%, depending on ICME phase, with GUMICS-4 values being mostly larger than those measured by either of the two spacecraft. Overall, δ is lower between GUMICS-4 and Cluster than between GUMICS-4 and Geotail. Largest δ between GUMICS-4 and Cluster in 2012 is created during the ICME sheath (59.2%), however, this phase creates lowest δ when comparing GUMICS-4 and Geotail (41.9%). The difference in δ between nominal solar wind conditions and ICME cloud phase is considerably lower for the 2012 event (61.4% and 66.6%) than for the 2014 event (55% and. 79.7%) when comparing GUMICS-4 and Geotail. Similar trend is observable if comparison between GUMICS-4 and Cluster is considered (37.3% and 52.7% for the 2012 event, 36.5% and 62.9% for the 2014 event), albeit with slightly lower magnitude. Moreover, while δ is quite similar regardless of Geotail position with respect to the magnetopause in both 2012 and 2014, it increases from 34.4% to 60.8% during the 2014 event between GUMICS-4 and Cluster. The standard deviations (SD) over the simulated time ranges using 0.5 $\mathrm{R_E}$ spatial resolutions are considerably lower on Geotail orbit (2012: 5.476, 2014: 6.564) than on Cluster orbit (2012: 25.054, 2014: 24.795).

5 Discussion

In this paper we study 1) how the magnetosphere responds to two ICME events with different characteristics by means of using the GUMICS-4 global MHD simulation, and 2) how accurately GUMICS-4 reproduces the effects of the two events. The 2012 event was stronger in terms of solar wind driver, the 2014 event being significantly weaker both in terms of solar wind speed and IMF magnitude. We considered both global and local parameters, including magnetopause nose position along the Sun-Earth line, total energy transferred from the solar wind into the magnetosphere, and the ionospheric cross-polar cap

potential (CPCP). Local measures include response of the magnetic field magnitude along the orbits of Cluster and Geotail spacecraft. The two ICME events were simulated using 0.5 $\mathrm{R_E}$ maximum spatial resolution. To test the effect of grid resolution enhancement on global dynamics, we simulated 6-hour subsets of both CME cloud periods with 0.25 $\mathrm{R_E}$ maximum spatial resolution. As an uncertainty metrics we use both relative difference magnitude δ and standard deviation SD.

Due to stronger solar wind driving, the 2012 event causes the magnetosphere to compress more than during the 2014 event, with the magnetopause moving Earthward at the onset of the 2012 ICME sheath and reaching 7 $\mathrm{R_E}$ distance from Earth, until moving Sunward at the onset of ICME magnetic cloud (see figure 6c). Both ICMEs are preceded by low IMF B_Z and solar wind dynamic pressure, with the 2014 missing high amplitude fluctuations before ICME cloud due to absence of separate ICME sheath. Despite this, the movement of the magnetopause is similarly Earthward prior to the cloud, reaching 9.5 $\mathrm{R_E}$ just before the onset of the cloud (see figure 7c). During the cloud however, the orientation of the IMF slowly rotates from southward to northward and the magnetopause is in constant Sunward (Earthward) motion in 2012 (2014). While the polarity of the IMF changes before the end of the ICME in 2012, it changes from southward to northward only after the end of the ICME in 2014.

The magnetopause nose location in GUMICS-4 is identified as a single grid point from the maximum value of J_Y along the Sun-Earth line. Location deviations in response to solar wind driving in the GUMICS-4 results is dependent on the driver intensity: Stronger driving during the 2012 CME magnetic cloud leads to larger relative difference magnitude δ (2012: 8.0% δ on average) as compared to the Shue et al. (1997) model, whereas the agreement between the simulation and the empirical model is quite good (3.3% δ on average) during weaker driving during the 2014 event (figures 6 and 7). This view is further supported by standard deviations (SD): For the full simulation time range SD is 0.661 (0.321) in 2012 (2014). Average δ during nominal solar wind conditions is almost identical for both events: 2.5% for the 2012 event and 2.4% for the 2014 event.

Comparison of the magnetopause location between the 0.25 $\mathrm{R_E}$ (0.5 $\mathrm{R_E}$) resolution run and the Shue model show that the relative difference between the two is below 10% 92% (89%) of the 6 hour subset in 2012 (Figure 6c), while corresponding analysis of the 6 hour subset in 2014 (Figure 7c) yielded differences below 10% 100% of the time regardless of the resolution. It should be noted that, despite the relative difference magnitude is slightly lower for the 0.5 $\mathrm{R_E}$ resolution run than for the 0.25 $\mathrm{R_E}$ resolution run for both the 2012 (4.9% and 5.6%) and the 2014 (3.2% and 4.5%) events, the 0.25 $\mathrm{R_E}$ run reaches better agreement with the Shue model especially when the magnetopause is moving during high solar wind driving in July 16, 01:00 UT (Figure 6c).

When spatial resolution is increased, gradient quantities such as J_Y have sharper profiles and therefore larger values (Janhunen et al., 2012). As it is the maximum value of J_Y that we use to locate the magnetopause nose, the nose position evaluation in the lower resolution runs is more ambiguous both due to the larger spread of the current and due to the larger grid cell size. This may lead to changes in the maximum value up to several $\mathrm{R_E}$ over short time periods in response to upstream fluctuations. In the finer resolution runs, J_Y distribution is sharper, which leads to lesser fluctuations in the maximum value determination. However, the differences between the two grid resolutions occur only under rapidly varying solar wind or very low solar wind density conditions.

The empirical models developed by Shue et al. (Shue et al., 1997, 1998) are based on statistical analysis of large number of spacecraft measurements of plasma and magnetic field during magnetopause crossings. While the Shue et al. (1997) model is optimized for moderate upstream conditions, the Shue et al. (1998) targets especially stronger driving periods. However, we computed the difference in the magnetopause position between the two models and found that it is mostly less than 0.1 $\mathrm{R_E}$ with maximum difference of 0.4 $\mathrm{R_E}$, with Shue et al. (1997) model predicting more sunward magnetopause nose. Because of the small difference at the magnetopause nose, we have only used Shue et al. (1997) model in our study. Our results agree with previous papers (Palmroth et al., 2003; Lakka et al., 2017), with the latter reporting 3.4% average relative difference between the Shue model and GUMICS-4. Moreover, according to Gordeev et al. (2015), global MHD models are very close to each other in terms of predicting magnetopause standoff distance.

Differences in the magnetopause location do not necessarily translate into differences in global measures, as can be seen from figures 6d and 7d, which show the time evolution of the energy transferred from the solar wind through the magnetopause surface. The response of the total energy E_{tot} during both ICME cloud periods is quite similar regardless of the used grid resolution. As an integrated quantity, energy entry is a better indicator of the true physical processes of GUMICS-4 solution and does not suffer from dependence on grid resolution like the maximum J_Y (Janhunen et al., 2012). Therefore, in analyses of simulation results, it would be better to consider such global integrated quantities, even if they have no direct observational counterparts. This can be seen in figures 6d and 7d, with large differences between GUMICS-4 and the ϵ-parameter (Perreault and Akasofu, 1978) in energy transferred from the solar wind into the magnetosphere in both 2012 and 2014. However, standard deviations show that GUMICS-4 reproduces temporal evolution of the ϵ-parameter better during low solar wind driving (2014) than during high driving (2012), as the respective SD values are 0.725 and 2.263. Moreover, our results are mostly of the same order of magnitude compared to what was obtained by Palmroth et al. (2003) by using plasma flow streamlines for computing the magnetopause surface from GUMICS-4 results.

In the ionosphere, the cross-polar cap potential value is dependent on the grid resolution, with higher resolution yielding higher polar cap potential values. For the 2012 event the average δ during July 15, 21:00 UT – July 16, 03:00 UT is 31.2% with 0.5 $\mathrm{R_E}$ resolution, while with 0.25 $\mathrm{R_E}$ resolution it is 16.3%. The 2014 event features similar trend, as the δ values are 70% and 27% for the corresponding 6 hour stages using low and high resolutions. As can be seen in Figure 6e, the difference between the two resolution runs can be up to 30% during the first 4 hours of the 6 hour stage, until the CPCP obtained from the 0.5 $\mathrm{R_E}$ resolution run starts to increase and eventually catches the 0.25 $\mathrm{R_E}$ resolution run at 03:00 UT. Similar evolution is absent during the 2014 event (Figure 7e). In comparison with the PCI index (Ridley and Kihn, 2004), standard deviation is considerably lower for the 2014 event (5.107) than for the 2012 event (15.838). Thus, at least two factors contribute to the ionospheric coupling: Grid resolution and intensity of solar wind driving. Considering that the SD values are clearly higher than e.g. the corresponding energy transfer values, and that the PCI index considers only the northern hemisphere, the PCI index may not provide the most accurate reference for GUMICS-4. However, both considerable difference between GUMICS-4 and the PCI and the dependence on grid resolution agree with previous studies (e.g. Lakka et al., 2018). Moreover, Gordeev et al. (2015) reported differences of order tens of kV between GUMICS-4 and other GMHD models.

The polar cap structure and the distribution of the FAC do not change much in either of the simulations, thus suggesting that the coupling of the magnetosphere and the ionosphere remains relatively constant. As is shown in figures 10a–10b, the region 1 currents are clearly visible, while the region 2 currents get stronger only by enhancing the grid resolution in the MHD region (Janhunen et al., 2012). However, the upstream conditions change considerably from 01:00 to 03:00, with the upstream Alfvén Mach number decreasing from 1.9 to 0.6, suggesting that polar cap potential saturation mechanisms are likely to take place (Ridley, 2007; Wilder et al., 2015; Lakka et al., 2018). Considering that GUMICS-4 reproduces saturation with both 0.5 $\mathrm{R_E}$ (this paper) and 0.25 $\mathrm{R_E}$ resolutions (Lakka et al., 2018), it is apparent that the FAC influence on the dayside magnetospheric magnetic field do not contribute to the saturation effect. However, to actually prove it is beyond te scope of the current paper. We therefore conclude that the increase of the CPCP during the 0.5 $\mathrm{R_E}$ simulation run is caused by processes outside of the magnetosphere, likely in the magnetosheath, and that GUMICS-4 responds differently to low Alfvén Mach number solar wind depending on grid resolution.

Figures 8 and 9 illustrate the CPCP as a function of the solar wind E_Y component. Color-coded are the IMF magnitude in figures 8a and 9a, the solar wind speed in figures 8b and 9b, and the upstream Alfvén Mach number in figures 8c and 9c. Nominal solar wind conditions before and after the actual ICME events as well as the ICME sheath and cloud periods are considered separately. We note that only results from the lower spatial resolution (0.5 $\mathrm{R_E}$) runs are included in the figures. Consistent with earlier studies, Figure 8 shows saturation of the CPCP during high solar wind driving (see e.g. Shepherd (2007); Russell et al. (2001)): With nominal solar wind conditions or during ICME sheath period the response of the CPCP to the upstream E_Y is rather linear, while for ICME cloud period the CPCP saturates, when $E_Y > 5\mathrm{mV/m}$. From Figure 8a it can be seen that the saturation occurs when $B > 12$ nT and Figure 8b shows that the increase of the CPCP in the linear regime depends on the upstream velocity in such a way that the increase is clearly higher for lower velocity values (cloud event), than for higher velocity values (sheath event and nominal conditions), as suggested by previous statistical (Newell et al., 2008) and numerical (Lopez et al., 2010) studies. The latter study proposes that this is because of the more rapid diversion of the solar wind flow in the pressure gradient dominated magnetosheath under faster solar wind, which leaves a smaller amount of plasma at the magnetic reconnection site.

The saturation of the CPCP is absent in Figure 9 due to the significantly weaker solar wind driving during the 2014 event (the upstream E_Y is below 4 $\mathrm{mV/m}$). This in turn leads to the upstream Alfvén Mach number to be on average 5.8 during the ICME cloud event. Lavraud and Borovsky (2008) suggests that when the Alfvén Mach number decreases below 4 and the overall magnetosheath plasma beta (p/p_B, where p is the plasma pressure and p_B the magnetic pressure) below 1, the magnetosheath force balance changes such that plasma flow streamlines are diverted away from the magnetic reconnection merging region in the dayside magnetopause (Lopez et al., 2010), which causes the CPCP saturation. However, the CPCP saturation limit of $M_A = 4$ is not necessarily the only governing parameter, as there is both observational evidence with large M_A values (up to 7.3) (Myllys et al., 2016) and simulation results indicating saturation at low but above $M_A = 1$ values (this study). Nonetheless, our results suggest that the saturation of the CPCP is dependent on the upstream M_A in such a way that M_A needs to be below 4 for the saturation to occur.

An interesting aspect is that the CPCP does not reach its maximum simultaneously with E_Y, i.e. the CPCP is largest with moderate E_Y (5–6 $\mathrm{mV/m}$) (see Figure 8). As E_Y increases to 11 $\mathrm{mV/m}$, the CPCP decreases from 70 kV to 40 kV. This is actually apparent in Figure 1h as well: The absolute values of both B_Z and V_X reach their maximum values a few hours after the onset of the magnetic cloud, which is at 6.54 UT, July 15. However, the CPCP is at that time quite moderate, about 40 kV, and does not reach its maximum until July 16, when both B_Z and V_X have already reduced significantly. Thus the CPCP overshoots in Figure 8, a feature that was not observed in a GUMICS-4 study by Lakka et al. (2018) using artificial solar wind input consisting of relatively high density and constant driving parameters.

The performance of GUMICS-4 was put to test by means of comparing the magnetic field magnitude $|B|$ to in-situ data of Cluster and Geotail satellites. GUMICS-4 values are mostly larger than those measured by either of the two spacecraft. Tables 4 and 5 show the relative difference magnitude in $|B|$ for both comparison pairs. Overall, δ is lower between GUMICS-4 and Cluster, than between GUMICS-4 and Geotail.

During both events, $|B|$ is increased during ICMEs, especially their magnetic cloud counterparts. During the 2012 ICME sheath both Cluster and Geotail record fluctuating $|B|$ until the onset of the cloud. Albeit missing sheath in 2014, magnetic field magnitude measured by Cluster fluctuates as well prior to the cloud. At the same time (April 29, 15:00 UT) $|B|$ measured by Geotail decreases sharply.

Largest δ between GUMICS-4 and Cluster during the 2012 event is created during the ICME sheath (59.2%), however, this period creates lowest δ when comparing GUMICS-4 and Geotail (41.9%). The difference in δ between nominal solar wind conditions and ICME cloud is considerably lower for the 2012 event (61.4% and 66.6%) than for the 2014 event (55% and. 79.7%) when comparing GUMICS-4 and Geotail. Similar trend is observable if comparison between GUMICS-4 and Cluster is considered, (37.3% and 52.7% for the 2012 event, 36.5% and 62.9% for the 2014 event) albeit with slightly lower magnitude. Moreover, while δ is quite similar regardless of Geotail position with respect to the magnetopause in both 2012 and 2014, it increases from 34.4% to 60.8% during the 2014 event between GUMICS-4 and Cluster.

As the relative difference magnitudes δ are mostly comparable regardless of which of the two events is considered, yet considerably lower for Cluster than Geotail, it is apparent that δ is affected more by the spacecraft orbit and, to a lesser extent, the upstream conditions. This is further manifested by the average δ over time the spacecraft spends inside and outside the magnetosphere. In table 5 average δ in 2014 when the spacecraft is inside the magnetosphere is 34.4% while the value is 60.8% when Cluster is outside the magnetosphere. Comparison between Geotail and GUMICS-4 suggests the same, with 58.2% (65.1%) average δ when the spacecraft is inside (outside) the magnetosphere. Computed standard deviations reveal that, over the entire simulation periods, the temporal evolution of GUMICS-4 magnetic field magnitude predictions is closer to Geotail measurements (2012: SD = 5.476, 2014:SD = 6.564, equatorial orbit) than Cluster measurements (2012: SD = 25.054, 2014: SD = 24.795, polar orbit) for both events. It should be noted that the times when Cluster is closer than 3.7 $\mathrm{R_E}$ to Earth are ignored when computing δ and SD values due to the inner boundary of the GUMICS-4 MHD region, which is located at 3.7 $\mathrm{R_E}$.

We conclude that for both events, $|B|$ predicted by GUMICS-4 is closer to Cluster observations, which feature high magnetic field magnitude outside the plasma sheet. However, the SD values suggest that GUMICS-4 reproduces temporal evolution of $|B|$ better at Geotail, which is much further away from the Earth than Cluster, and resides mostly in the lobe and on the

boundary layer. We also computed standard deviations for Cluster orbit when the S/C is both further and closer than 5 $\mathrm{R_E}$ away from the center of the Earth. SD for further than 5 $\mathrm{R_E}$ is 22.984 (19.666) for the 2012 (2014) event, while for closer than 5 $\mathrm{R_E}$ the SD is 106.337 (104.605) for the 2012 (2014) event. If these calculations are repeated for 6 $\mathrm{R_E}$ distance, the SD values are 14.390 (15.282) when the S/C is further in 2012 (2014), and 104.618 (88.423) when the S/C is closer in 2012 (2014). Thus, the temporal evolutions agree better when Cluster is further away from the Earth.

The differences are most likely not caused by grid cell size variations due to the adaptive grid of GUMICS-4, because the average δ values over simulated 6-hour stages (see tables 4 and 5) are quite similar for both resolutions. Also, most of the difference is created during the first hours of the 6 hour stage, during which the 0.25 $\mathrm{R_E}$ run may not have fully eliminated the effects of simulation initialization, which can prevail hours (Lakka et al., 2017). Moreover, the adaptive grid of GUMICS-4 is enhanced the most near the dayside magnetopause. Both events show signs of increased $|\delta|$ near the dayside magnetopause (edges of yellow-shaded regions in figures 4 and 5), further manifesting inaccuracies in determining the magnetopause in GUMICS-4.

6 Conclusions

The results of this paper can be summarized as follows:

(1) Enhancing spatial resolution of the magnetosphere in GUMICS-4 affects the accuracy of the determination of the the magnetopause subsolar point. Global measures, such as energy transferred from the solar wind into the magnetosphere, are not affected. The cross-polar cap potential can be affected significantly, with up to over factor of 2 difference between simulations using different spatial resolutions for the magnetosphere.

(2) Our results show signs of cross-polar cap potential saturation during low upstream Alfvén Mach number. GUMICS-4 responds differently to low Alfvén Mach number solar wind, which may affect the saturation phenomena. This may lead to grid size effects to polar cap saturation in MHD simulations.

(3) Overall time evolution of the magnetic field magnitude $|B|$ predicted by GUMICS-4 agrees observed $|B|$ better when the magnetic field magnitude is high. GUMICS-4 is generally prone to overestimate the field magnitude. Due to inaccuracies in the magnetopause subsolar point determination, comparison between GUMICS-4 and in-situ data should be done cautiously when the spacecraft is near the magnetopause.

Data availability. Solar wind data are freely available from the NASA/GSFC Omniweb server (https://omniweb.gsfc.nasa.gov/). Solar energetic particle data are freely available from the NOAA NCEI Space Weather data access (https://www.ngdc.noaa.gov/stp/satellite/goes/index.html).

Competing interests. The authors declare that they have no conflict of interest.

Acknowledgements. The calculations presented above were performed using computer resources within the Aalto University School of Science "Science-IT" project. This project was funded by the Academy of Finland grants #1267087, #288472, and #310444. We acknowledge use of NASA/GSFC's Space Physics Data Facility's OMNIWeb service, and OMNI data. Solar energetic particle data supplied courtesy of ngdc.noaa.gov.

References

Akasofu, S. I.: Energy coupling between the solar wind and the magnetosphere, Space Science Reviews, 28, 121–190, https://doi.org/10.1007/BF00218810, https://doi.org/10.1007/BF00218810, 1981.

Axford, W. I. and Hines, C. O.: A UNIFYING THEORY OF HIGH-LATITUDE GEOPHYSICAL PHENOMENA AND GEOMAGNETIC STORMS, Canadian Journal of Physics, 39, 1433–1464, https://doi.org/10.1139/p61-172, http://dx.doi.org/10.1139/p61-172, 1961.

Birn, J., Drake, J. F., Shay, M. A., Rogers, B. N., Denton, R. E., Hesse, M., Kuznetsova, M., Ma, Z. W., Bhattacharjee, A., Otto, A., and Pritchett, P. L.: Geospace Environmental Modeling (GEM) Magnetic Reconnection Challenge, Journal of Geophysical Research: Space Physics, 106, 3715–3719, https://doi.org/10.1029/1999JA900449, http://dx.doi.org/10.1029/1999JA900449, 2001.

Burlaga, L., Sittler, E., Mariani, F., , and Schwenn, R.: Magnetic loop behind an interplanetary shock: Voyager, Helios, and IMP 8 observations, Journal of Geophysical Research: Space Physics, 86, 6673–6684, https://doi.org/10.1029/JA086iA08p06673, https://agupubs.onlinelibrary.wiley.com/doi/abs/10.1029/JA086iA08p06673, 1981.

Dungey, J. W.: Interplanetary Magnetic Field and the Auroral Zones, Phys. Rev. Lett., 6, 47–48, https://doi.org/10.1103/PhysRevLett.6.47, http://link.aps.org/doi/10.1103/PhysRevLett.6.47, 1961.

Goldstein, R., Neugebauer, M., and Clay, D.: A statistical study of coronal mass ejection plasma flows, Journal of Geophysical Research: Space Physics, 103, 4761–4766, https://doi.org/10.1029/97JA03663, https://agupubs.onlinelibrary.wiley.com/doi/abs/10.1029/97JA03663, 1998.

Gordeev, E., Sergeev, V., Honkonen, I., Kuznetsova, M., Rastätter, L., Palmroth, M., Janhunen, P., Tóth, G., Lyon, J., and Wiltberger, M.: Assessing the performance of community-available global MHD models using key system parameters and empirical relationships, Space Weather, 13, 868–884, https://doi.org/10.1002/2015SW001307, http://dx.doi.org/10.1002/2015SW001307, 2015SW001307, 2015.

Gosling, J. T.: Coronal Mass Ejections and Magnetic Flux Ropes in Interplanetary Space, pp. 343–364, American Geophysical Union (AGU), https://doi.org/10.1029/GM058p0343, https://agupubs.onlinelibrary.wiley.com/doi/abs/10.1029/GM058p0343, 1990.

Gosling, J. T., Pizzo, V., and Bam, S. J.: Anomalously low proton temperatures in the solar wind following interplanetary shock waves—evidence for magnetic bottles?, Journal of Geophysical Research, 78, 2001–2009, https://doi.org/10.1029/JA078i013p02001, https://agupubs.onlinelibrary.wiley.com/doi/abs/10.1029/JA078i013p02001, 1973.

Gosling, J. T., McComas, D. J., Phillips, J. L., and Bame, S. J.: Geomagnetic activity associated with earth passage of interplanetary shock disturbances and coronal mass ejections, Journal of Geophysical Research: Space Physics, 96, 7831–7839, https://doi.org/10.1029/91JA00316, https://agupubs.onlinelibrary.wiley.com/doi/abs/10.1029/91JA00316, 1991.

Hirshberg, J. and Colburn, D. S.: Interplanetary field and geomagnetic variations—a unifield view, Planetary and Space Science, 17, 1183 – 1206, https://doi.org/https://doi.org/10.1016/0032-0633(69)90010-5, 1969.

Hirshberg, J., Bame, S. J., and Robbins, D. E.: Solar flares and solar wind helium enrichments: July 1965-July 1967, Solar Physics, 23, 467–486, https://doi.org/10.1007/BF00148109, https://doi.org/10.1007/BF00148109, 1972.

Honkonen, I., Rastätter, L., Grocott, A., Pulkkinen, A., Palmroth, M., Raeder, J., Ridley, A. J., and Wiltberger, M.: On the performance of global magnetohydrodynamic models in the Earth's magnetosphere, Space Weather, 11, 313–326, https://doi.org/10.1002/swe.20055, http://dx.doi.org/10.1002/swe.20055, 2013.

Huttunen, K. E. J. and Koskinen, H. E. J.: Importance of post-shock streams and sheath region as drivers of intense magnetospheric storms and high-latitude activity, Annales Geophysicae, 22, 1729–1738, https://hal.archives-ouvertes.fr/hal-00317357, 2004.

Huttunen, K. E. J., Koskinen, H. E. J., and Schwenn, R.: Variability of magnetospheric storms driven by different solar wind perturbations, Journal of Geophysical Research: Space Physics, 107, SMP 20–1–SMP 20–8, 2002.

Janhunen, P.: GUMICS-3 A Global Ionosphere-Magnetosphere Coupling Simulation with High Ionospheric Resolution, in: Environment Modeling for Space-Based Applications, edited by Guyenne, T.-D. and Hilgers, A., vol. 392 of *ESA Special Publication*, p. 233, 1996.

Janhunen, P. and Huuskonen, A.: A numerical ionosphere-magnetosphere coupling model with variable conductivities, Journal of Geophysical Research: Space Physics, 98, 9519–9530, https://doi.org/10.1029/92JA02973, http://dx.doi.org/10.1029/92JA02973, 1993.

Janhunen, P., Palmroth, M., Laitinen, T., Honkonen, I., Juusola, L., Facskó, G., and Pulkkinen, T.: The GUMICS-4 global {MHD} magnetosphere–ionosphere coupling simulation, Journal of Atmospheric and Solar-Terrestrial Physics, 80, 48 – 59, https://doi.org/http://dx.doi.org/10.1016/j.jastp.2012.03.006, http://www.sciencedirect.com/science/article/pii/S1364682612000909, 2012.

Jianpeng, G., Xueshang, F., Jie, Z., Pingbing, Z., and Changqing, X.: Statistical properties and geoefficiency of interplanetary coronal mass ejections and their sheaths during intense geomagnetic storms, Journal of Geophysical Research: Space Physics, 115, https://doi.org/10.1029/2009JA015140, https://agupubs.onlinelibrary.wiley.com/doi/abs/10.1029/2009JA015140, 2010.

J.L. Lions, G. C.: Handbook of Numerical Analysis. Solution of Equations in Rn (Part 3), Techniques of Scientific Computing (Part 3), vol. Volume 7, North-Holland, 1 edn., 2000.

Johnson, J. R. and Cheng, C. Z.: Kinetic Alfvén waves and plasma transport at the magnetopause, Geophysical Research Letters, 24, 1423–1426, https://doi.org/10.1029/97GL01333, http://dx.doi.org/10.1029/97GL01333, 1997.

Juusola, L., Facskó, G., Honkonen, I., Janhunen, P., Vanhamäki, H., Kauristie, K., Laitinen, T. V., Milan, S. E., Palmroth, M., Tanskanen, E. I., and Viljanen, A.: Statistical comparison of seasonal variations in the GUMICS-4 global MHD model ionosphere and measurements, Space Weather, 12, 582–600, https://doi.org/10.1002/2014SW001082, 2014.

Kilpua, E., Isavnin, A., Vourlidas, A., Koskinen, H., and Rodriguez, L.: On the relationship between interplanetary coronal mass ejections and magnetic clouds, 31, 1251–1265, 2013.

Kilpua, E., Koskinen, H. E. J., and Pulkkinen, T. I.: Coronal mass ejections and their sheath regions in interplanetary space, Living Reviews in Solar Physics, 14, 5, https://doi.org/10.1007/s41116-017-0009-6, https://doi.org/10.1007/s41116-017-0009-6, 2017a.

Kilpua, E. K. J., Balogh, A., von Steiger, R., and Liu, Y. D.: Geoeffective Properties of Solar Transients and Stream Interaction Regions, Space Science Reviews, 212, 1271–1314, https://doi.org/10.1007/s11214-017-0411-3, https://doi.org/10.1007/s11214-017-0411-3, 2017b.

Koustov, A. V., Khachikjan, G. Y., Makarevich, R. A., and Bryant, C.: On the SuperDARN cross polar cap potential saturation effect, Annales Geophysicae, 27, 3755–3764, https://doi.org/10.5194/angeo-27-3755-2009, 2009.

Kubota, Y., Nagatsuma, T., Den, M., Tanaka, T., and Fujita, S.: Polar cap potential saturation during the Bastille Day storm event using global MHD simulation, Journal of Geophysical Research: Space Physics, 122, 4398–4409, https://doi.org/10.1002/2016JA023851, http://dx.doi.org/10.1002/2016JA023851, 2016JA023851, 2017.

Lakka, A., Pulkkinen, T. I., Dimmock, A. P., Osmane, A., Honkonen, I., Palmroth, M., and Janhunen, P.: The impact on global magnetohydrodynamic simulations from varying initialisation methods: results from GUMICS-4, Annales Geophysicae, 35, 907–922, https://doi.org/10.5194/angeo-35-907-2017, https://www.ann-geophys.net/35/907/2017/, 2017.

Lakka, A., Pulkkinen, T. I., Dimmock, A. P., Myllys, M., Honkonen, I., and Palmroth, M.: The Cross-Polar Cap Saturation in GUMICS-4 During High Solar Wind Driving, Journal of Geophysical Research: Space Physics, 0, https://doi.org/10.1002/2017JA025054, https://agupubs.onlinelibrary.wiley.com/doi/abs/10.1002/2017JA025054, 2018.

Lavraud, B. and Borovsky, J. E.: Altered solar wind-magnetosphere interaction at low Mach numbers: Coronal mass ejections, Journal of Geophysical Research: Space Physics, 113, n/a–n/a, https://doi.org/10.1029/2008JA013192, http://dx.doi.org/10.1029/2008JA013192, a00B08, 2008.

Lopez, R. E., Bruntz, R., Mitchell, E. J., Wiltberger, M., Lyon, J. G., and Merkin, V. G.: Role of magnetosheath force balance in regulating the dayside reconnection potential, Journal of Geophysical Research: Space Physics, 115, n/a–n/a, https://doi.org/10.1029/2009JA014597, http://dx.doi.org/10.1029/2009JA014597, a12216, 2010.

Myllys, M., Kilpua, E., Lavraud, B., and Pulkkinen, T. I.: Solar wind-magnetosphere coupling efficiency during ejecta and sheath-driven geomagnetic storms, p. 4378–4396, https://doi.org/10.1002/2016JA022407, http://urn.fi/URN:NBN:fi:aalto-201610124801, 2016.

Myllys, M., Kipua, E. K. J., and Lavraud, B.: Interplay of solar wind parameters and physical mechanisms producing the saturation of the cross polar cap potential, Geophysical Research Letters, 44, 3019–3027, https://doi.org/10.1002/2017GL072676, https://agupubs.onlinelibrary.wiley.com/doi/abs/10.1002/2017GL072676, 2017.

Newell, P. T., Sotirelis, T., Liou, K., and Rich, F. J.: Pairs of solar wind-magnetosphere coupling functions: Combining a merging term with a viscous term works best, Journal of Geophysical Research: Space Physics, 113, n/a–n/a, https://doi.org/10.1029/2007JA012825, http://dx.doi.org/10.1029/2007JA012825, a04218, 2008.

Nishida, A.: Coherence of geomagnetic DP 2 fluctuations with interplanetary magnetic variations, Journal of Geophysical Research, 73, 5549–5559, https://doi.org/10.1029/JA073i017p05549, http://dx.doi.org/10.1029/JA073i017p05549, 1968.

Nykyri, K. and Otto, A.: Plasma transport at the magnetospheric boundary due to reconnection in Kelvin-Helmholtz vortices, Geophysical Research Letters, 28, 3565–3568, https://doi.org/10.1029/2001GL013239, http://dx.doi.org/10.1029/2001GL013239, 2001.

Osmane, A., Dimmock, A., Naderpour, R., Pulkkinen, T., and Nykyri, K.: The impact of solar wind ULF B-z fluctuations on geomagnetic activity for viscous timescales during strongly northward and southward IMF, JOURNAL OF GEOPHYSICAL RESEARCH: SPACE PHYSICS, 120, 9307–9322, https://doi.org/10.1002/2015JA021505, 2015.

Palmroth, M., Pulkkinen, T. I., Janhunen, P., and Wu, C.-C.: Stormtime energy transfer in global MHD simulation, Journal of Geophysical Research: Space Physics, 108, n/a–n/a, https://doi.org/10.1029/2002JA009446, http://dx.doi.org/10.1029/2002JA009446, 1048, 2003.

Perreault, P. and Akasofu, S.-I.: A study of geomagnetic storms, Geophysical Journal of the Royal Astronomical Society, 54, 547–573, 1978.

Pulkkinen, A., Kuznetsova, M., Ridley, A., Raeder, J., Vapirev, A., Weimer, D., Weigel, R. S., Wiltberger, M., Millward, G., Rastätter, L., Hesse, M., Singer, H. J., and Chulaki, A.: Geospace Environment Modeling 2008–2009 Challenge: Ground magnetic field perturbations, Space Weather, 9, n/a–n/a, https://doi.org/10.1029/2010SW000600, http://dx.doi.org/10.1029/2010SW000600, s02004, 2011.

Pulkkinen, T. I., Partamies, N., Huttunen, K. E. J., Reeves, G. D., and Koskinen, H. E. J.: Differences in geomagnetic storms driven by magnetic clouds and ICME sheath regions, Geophysical Research Letters, 34, https://doi.org/10.1029/2006GL027775, https://agupubs.onlinelibrary.wiley.com/doi/abs/10.1029/2006GL027775, 2007.

Richardson, I. G. and Cane, H. V.: Identification of interplanetary coronal mass ejections at 1 AU using multiple solar wind plasma composition anomalies, Journal of Geophysical Research: Space Physics, 109, https://doi.org/10.1029/2004JA010598, https://agupubs.onlinelibrary.wiley.com/doi/abs/10.1029/2004JA010598, 2003.

Richardson, I. G. and Cane, H. V.: Solar wind drivers of geomagnetic storms during more than four solar cycles, J. Space Weather Space Clim., 2, A01, https://doi.org/10.1051/swsc/2012001, https://doi.org/10.1051/swsc/2012001, 2012.

Ridley, A. J.: A new formulation for the ionospheric cross polar cap potential including saturation effects, Annales Geophysicae, 23, 3533–3547, https://hal.archives-ouvertes.fr/hal-00318077, 2005.

Ridley, A. J.: Alfvén wings at Earth's magnetosphere under strong interplanetary magnetic fields, Annales Geophysicae, 25, 533–542, https://doi.org/10.5194/angeo-25-533-2007, http://www.ann-geophys.net/25/533/2007/, 2007.

Ridley, A. J. and Kihn, E. A.: Polar cap index comparisons with AMIE cross polar cap potential, electric field, and polar cap area, Geophysical Research Letters, 31, https://doi.org/10.1029/2003GL019113, https://agupubs.onlinelibrary.wiley.com/doi/abs/10.1029/2003GL019113, 2004.

Russell, C. T., Luhmann, J. G., and Lu, G.: Nonlinear response of the polar ionosphere to large values of the interplanetary electric field, Journal of Geophysical Research: Space Physics, 106, 18 495–18 504, https://doi.org/10.1029/2001JA900053, http://dx.doi.org/10.1029/2001JA900053, 2001.

Shepherd, S. G.: Polar cap potential saturation: Observations, theory, and modeling, Journal of Atmospheric and Solar-Terrestrial Physics, 69, 234–248, 2007.

Shue, J.-H., Chao, J. K., Fu, H. C., Russell, C. T., Song, P., Khurana, K. K., and Singer, H. J.: A new functional form to study the solar wind control of the magnetopause size and shape, Journal of Geophysical Research: Space Physics, 102, 9497–9511, https://doi.org/10.1029/97JA00196, http://dx.doi.org/10.1029/97JA00196, 1997.

Shue, J.-H., Song, P., Russell, C. T., Steinberg, J. T., Chao, J. K., Kokubun, S., Singer, H. J., Detman, T. R., Zastenker, G., Vaisberg, O. L., and Kawano, H.: Magnetopause location under extreme solar wind conditions, Journal of Geophysical Research: Space Physics, 103, 17 691–17 700, https://doi.org/10.1029/98JA01103, https://agupubs.onlinelibrary.wiley.com/doi/abs/10.1029/98JA01103, 1998.

Siscoe, G. L., Lotko, W., and Sonnerup, B. U.: A high-latitude, low-latitude boundary layer model of the convection current system, Journal of Geophysical Research: Space Physics, 96, 3487–3495, 1991.

Tanaka, T.: Finite Volume TVD Scheme on an Unstructured Grid System for Three-Dimensional MHD Simulation of Inhomogeneous Systems Including Strong Background Potential Fields, Journal of Computational Physics, 111, 381 – 389, https://doi.org/http://dx.doi.org/10.1006/jcph.1994.1071, http://www.sciencedirect.com/science/article/pii/S0021999184710710, 1994.

Tsurutani, B. T., Gonzalez, W. D., Tang, F., Akasofu, S. I., and Smith, E. J.: Origin of interplanetary southward magnetic fields responsible for major magnetic storms near solar maximum (1978–1979), Journal of Geophysical Research: Space Physics, 93, 8519–8531, https://doi.org/10.1029/JA093iA08p08519, https://agupubs.onlinelibrary.wiley.com/doi/abs/10.1029/JA093iA08p08519, 1988.

Wilder, F. D., Clauer, C. R., Baker, J. B. H., Cousins, E. P., and Hairston, M. R.: The nonlinear response of the polar cap potential under southward IMF: A statistical view, Journal of Geophysical Research: Space Physics, 116, n/a–n/a, https://doi.org/10.1029/2011JA016924, http://dx.doi.org/10.1029/2011JA016924, a12229, 2011.

Wilder, F. D., Eriksson, S., and Wiltberger, M.: The role of magnetic flux tube deformation and magnetosheath plasma beta in the saturation of the Region 1 field-aligned current system, Journal of Geophysical Research: Space Physics, 120, 2036–2051, https://doi.org/10.1002/2014JA020533, http://dx.doi.org/10.1002/2014JA020533, 2014JA020533, 2015.

Wu, C.-C., Fry, C. D., Wu, S. T., Dryer, M., and Liou, K.: Three-dimensional global simulation of interplanetary coronal mass ejection propagation from the Sun to the heliosphere: Solar event of 12 May 1997, Journal of Geophysical Research: Space Physics, 112, https://doi.org/10.1029/2006JA012211, https://agupubs.onlinelibrary.wiley.com/doi/abs/10.1029/2006JA012211, 2007.

Wu, C.-C., Liou, K., Vourlidas, A., Plunkett, S., Dryer, M., Wu, S. T., and Mewaldt, R. A.: Global magnetohydrodynamic simulation of the 15 March 2013 coronal mass ejection event—Interpretation of the 30–80 MeV proton flux, Journal of Geophysical Research: Space Physics, 121, 56–76, https://doi.org/10.1002/2015JA021051, https://agupubs.onlinelibrary.wiley.com/doi/abs/10.1002/2015JA021051, 2015.

Yermolaev, Y. I., Nikolaeva, N. S., Lodkina, I. G., and Yermolaev, M. Y.: Geoeffectiveness and efficiency of CIR, sheath, and ICME in generation of magnetic storms, Journal of Geophysical Research: Space Physics, 117, https://doi.org/10.1029/2011JA017139, https://agupubs.onlinelibrary.wiley.com/doi/abs/10.1029/2011JA017139, 2012.

Zhang, J., Poomvises, W., and Richardson, I. G.: Sizes and relative geoeffectiveness of interplanetary coronal mass ejections and the preceding shock sheaths during intense storms in 1996–2005, Geophysical Research Letters, 35, https://doi.org/10.1029/2007GL032045, https://agupubs.onlinelibrary.wiley.com/doi/abs/10.1029/2007GL032045, 2012.

Table 1. Summary of the event simulations within the current study.

Event year	Nominal solar wind [h]	Event date and time	Event length [h]	Resolution [R_E]
2012	9.9	18:53 UT, July 14 – 04:19 UT, July 17	57.4	0.5
2014	25.6	20:38 UT, April 29 – 17:51 UT, April 30	21.2	0.5
2012	0	21:00 UT, July 15 – 03:00 UT, July 16	6	0.25
2014	0	00:00 UT, April 30 – 06:00 UT, April 30	6	0.25

Table 2. Average relative difference magnitudes in the magnetopause nose position for given simulation phase.

Event year	Resolution [R_E]	Nominal SW [%]	Sheath [%]	Cloud [%]	6 hours [%]
2012	0.5	2.5	4.5	8.0	4.9
2014	0.5	2.4	-	3.3	3.2
2012	0.25	-	-	-	5.6
2014	0.25	-	-	-	4.5

Table 3. Average relative difference magnitudes in the cross-polar cap potential for given simulation phase.

Event year	Resolution [R_E]	Nominal SW [%]	Sheath [%]	Cloud [%]	6 hours [%]
2012	0.5	64.9	57.6	36.0	31.2
2014	0.5	46.9	-	69.2	70.0
2012	0.25	-	-	-	16.3
2014	0.25	-	-	-	27.0

Table 4. Geotail vs. GUMICS-4: Average relative difference magnitudes in the magnetic field magnitude for given simulation phase. SC inside/outside refers to sequences during which the spacecraft is inside/outside the magnetosphere according to figure 3.

Event year	Resolution [R_E]	Nominal SW [%]	Sheath [%]	Cloud [%]	SC inside [%]	SC outside [%]	6 hours [%]
2012	0.5	61.4	41.9	66.6	61.1	62.7	69.7
2014	0.5	55.0	-	79.7	58.2	65.1	80.5
2012	0.25	-	-	-	-	-	68.2
2014	0.25	-	-	-	-	-	64.8

Table 5. Cluster vs. GUMICS-4: Average relative difference magnitudes in the magnetic field magnitude for given simulation phase. SC inside/outside refers to sequences during which the spacecraft is inside/outside the magnetosphere according to figure 3.

Event year	Resolution [R_E]	Nominal SW [%]	Sheath [%]	Cloud [%]	SC inside [%]	SC outside [%]	6 hours [%]
2012	0.5	37.3	59.2	52.7	49.7	-	58.6
2014	0.5	36.5	-	62.9	34.4	60.8	49.7
2012	0.25	-	-	-	-	-	53.0
2014	0.25	-	-	-	-	-	50.0

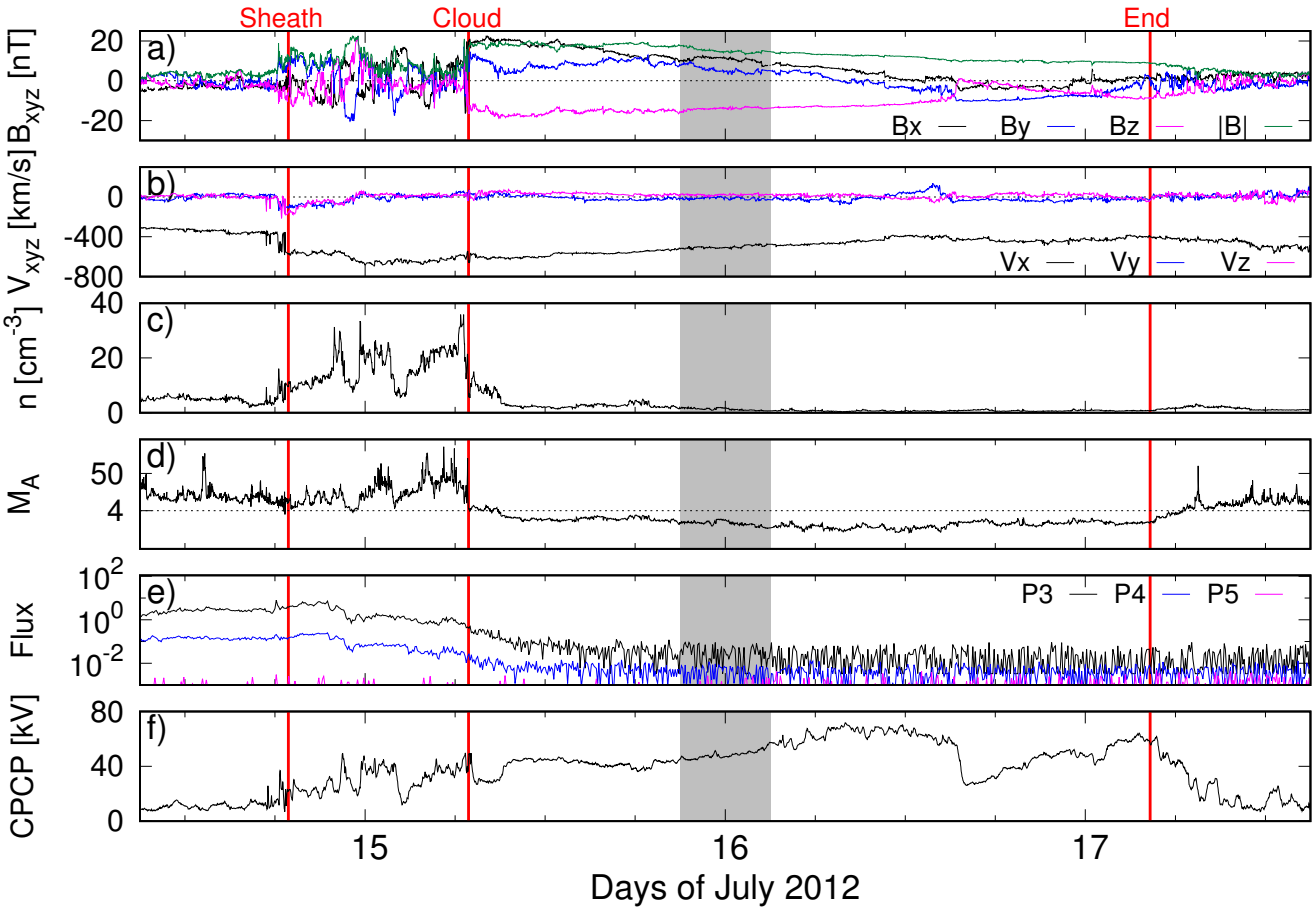

Figure 1. Solar wind and IMF conditions during July 14 09:00 UT – July 17 15:00 UT, 2012. Panels from top to bottom: a) IMF components B_X, B_Y and B_Z and the IMF magntiude in nT, b) plasma velocity components V_X, V_Y and V_Z in km/s, c) plasma number density n in cm^{-3}, d) upstream Alfvén Mach number M_A ($M_A = 4$ is marked with dotted line), e) GOES-15 geostationary orbit proton fluxes for three energy channels between 8–80 MeV, and f) the ionospheric cross-polar cap potential from GUMICS-4. Data in panels a–d is measured by ACE/Wind. Vertical red lines indicate onset of the ICME sheath/magnetic cloud or the end of the ICME event. Grey background shows the part of the ICME event that is simulated using both 0.25 and 0.5 R_E as a maximum spatial resolution.

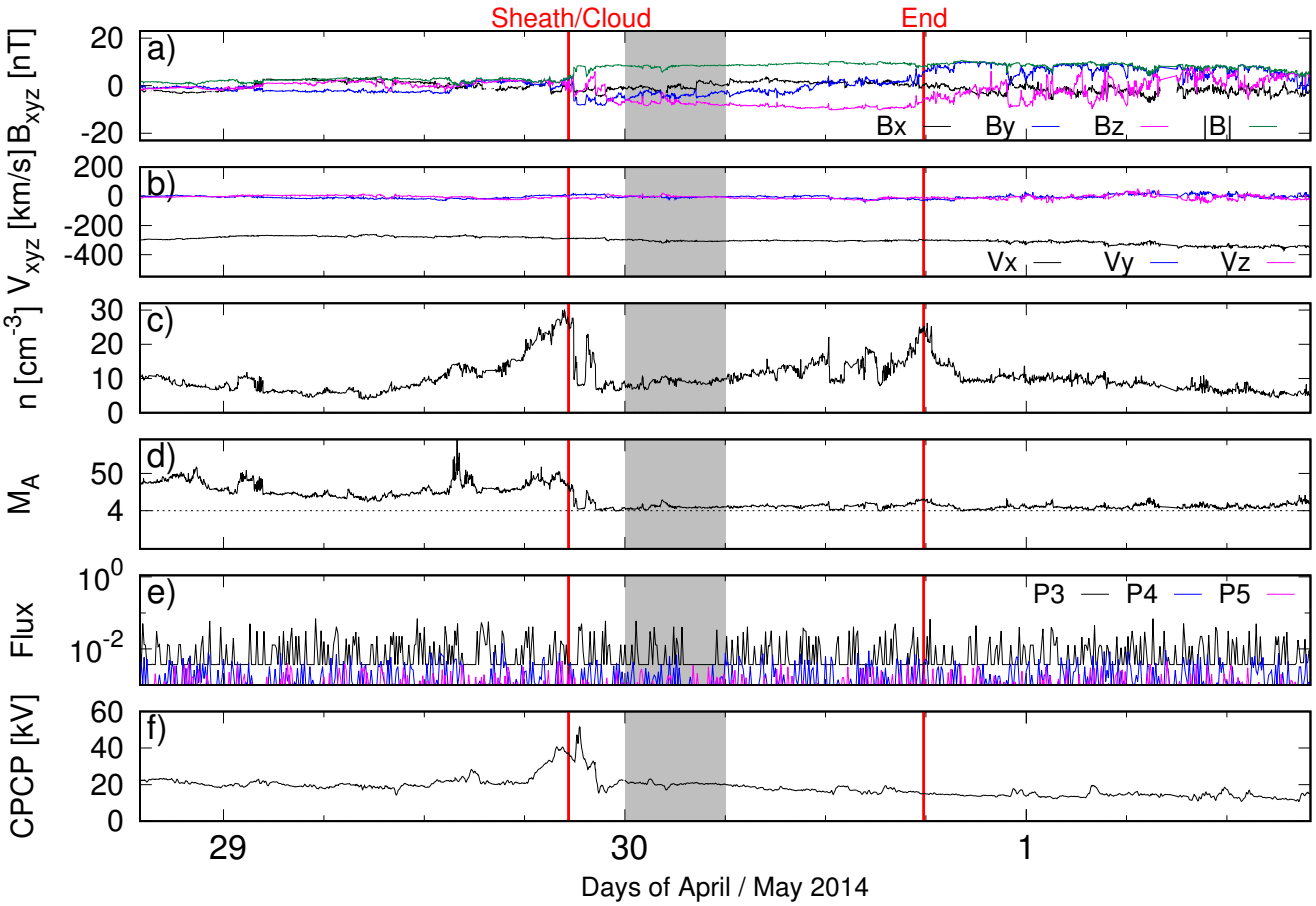

Figure 2. Solar wind and IMF conditions during April 28 19:00 UT – May 1 17:00 UT, 2014. Panels from top to bottom: a) IMF components B_X, B_Y and B_Z and the IMF magntiude in nT, b) plasma velocity components V_X, V_Y and V_Z in km/s, c) plasma number density n in cm^{-3}, d) upstream Alfvén Mach number M_A ($M_A = 4$ is marked with dotted line), e) GOES-15 geostationary orbit proton fluxes for three energy channels between 8–80 MeV, and f) the ionospheric cross-polar cap potential from GUMICS-4. Data in panels a–d is measured by ACE/Wind. Vertical red lines indicate onset of the ICME sheath/magnetic cloud or the end of the ICME event. Grey background shows the part of the ICME event that is simulated using both 0.25 and 0.5 R_E as a maximum spatial resolution.

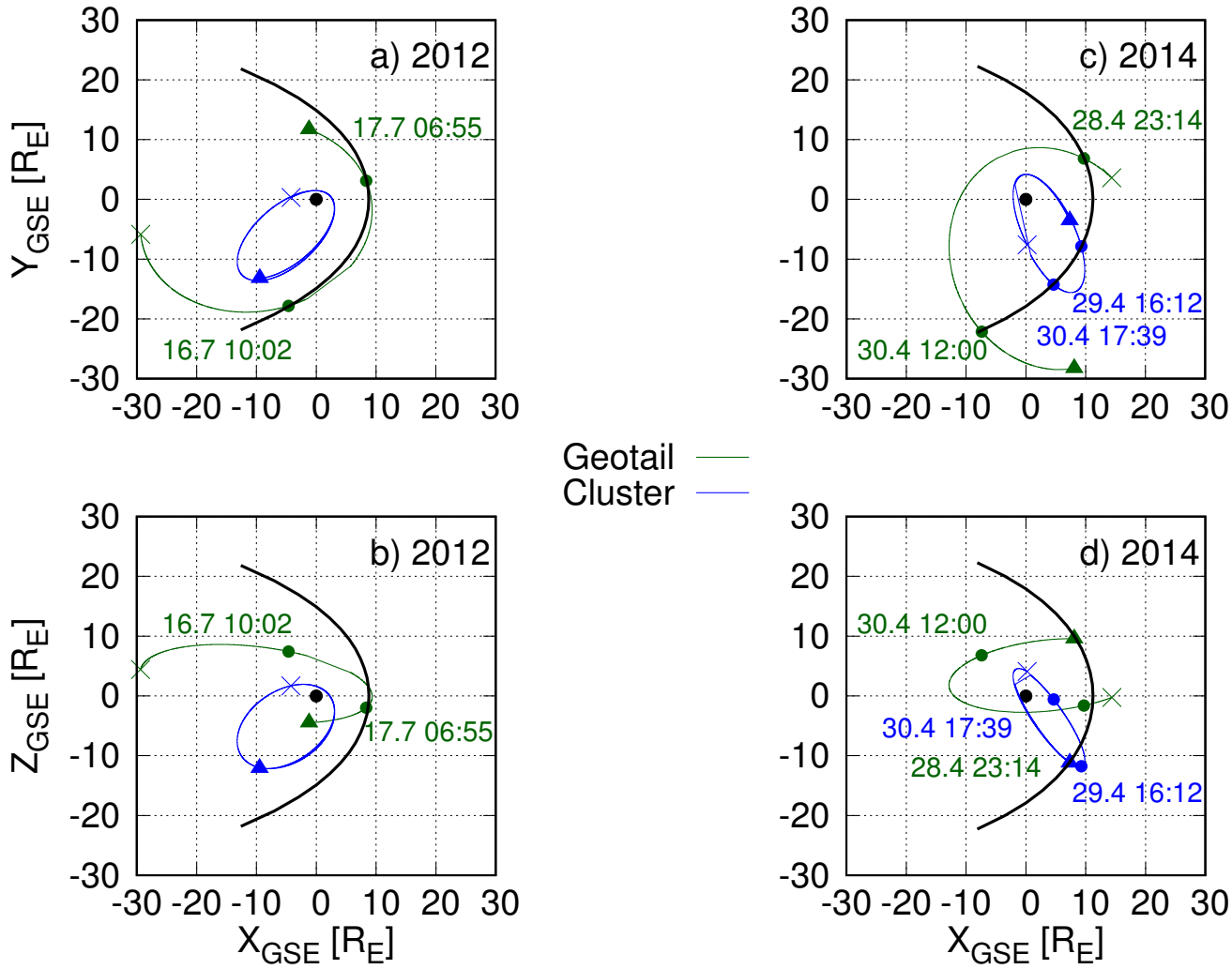

Figure 3. Orbits of Cluster 1 (blue) and Geotail (green) satellites during July 14 09:00 UT – July 17 15:00 UT, 2012 (panels a and b) and during April 28 19:00 UT – May 1 17:00 UT, 2014 (panels c and d). Orbits are shown on the XY plane in panels a and c and on the XZ plane in panels b and d. The coordinate system is GSE. The most earthward position of the Shue magnetopause during both time intervals is drawn in black. Start and end points of the time intervals are marked with a cross and a triangle, respectively. The points along the satellite orbits between which the spacecraft may encounter magnetopause crossings are marked with dots.

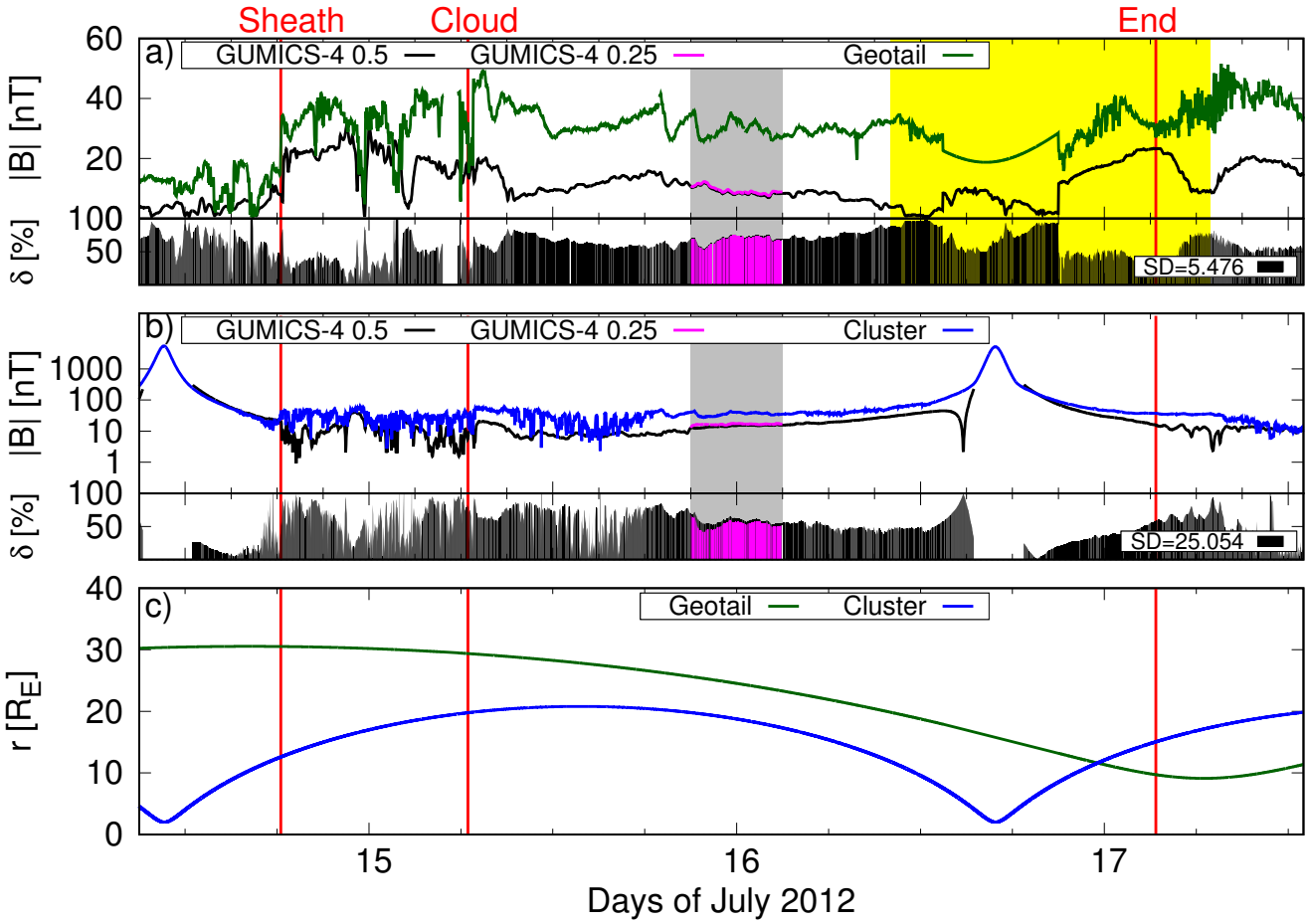

Figure 4. The time series of the magnetic field magnitude $|B|$ along the orbits of Geotail (panel a) and Cluster 1 (panel b) during July 14 09:00 UT – July 17 15:00 UT, 2012 as measured by Geotail (green) and Cluster 1 (blue) and predicted by GUMICS-4 (black and magenta). Black and magenta curves in panels a–b show GUMICS-4 results with maximum spatial resolution of 0.5 (black) and 0.25 (magenta) $\mathrm{R_E}$. Panel c: Radial distance of both spacecraft from the center of the Earth. The relative difference magnitude in $|B|$ between GUMICS-4 and the observation is given in panels a and b. Yellow-shaded regions indicate approximate time intervals when satellite may exit the magnetosphere. Grey-shaded regions show the part of the ICME event simulated also using 0.25 $\mathrm{R_E}$ maximum spatial resolution. Standard deviations (SD) for observation vs. GUMICS-4 (0.5 $\mathrm{R_E}$ resolution) datasets are given in panels a and b.

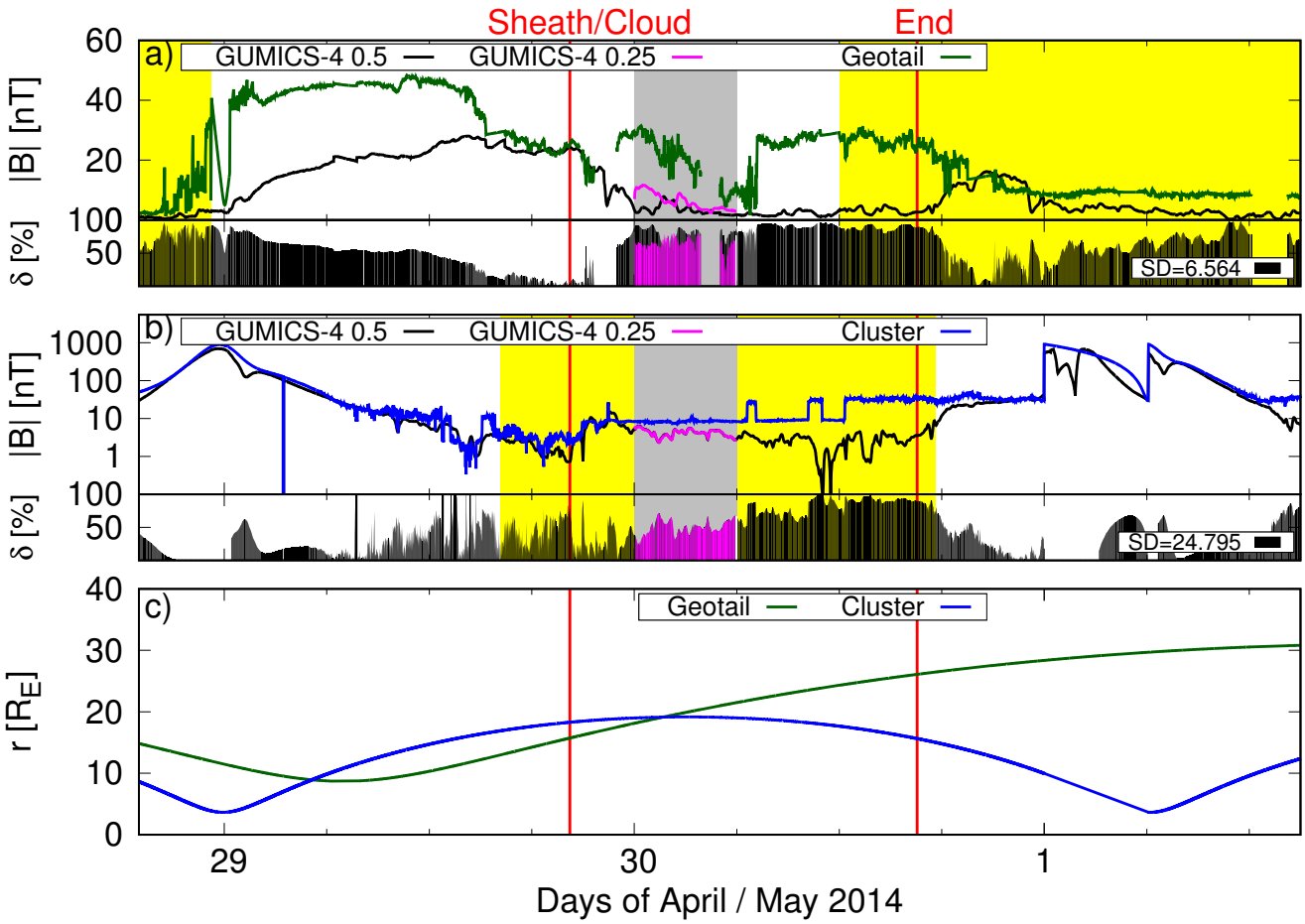

Figure 5. The time series of the magnetic field magnitude $|B|$ along the orbits of Geotail (panel a) and Cluster 1 (panel b) during April 28 19:00 UT – May 1 17:00 UT, 2014 as measured by Geotail (green) and Cluster 1 (blue) and predicted by GUMICS-4 (black and magenta). Black and magenta curves in panels a–b show GUMICS-4 results with maximum spatial resolution of 0.5 (black) and 0.25 (magenta) $\mathrm{R_E}$. Panel c: Radial distance of both spacecraft from the center of the Earth. The relative difference magnitude in $|B|$ between GUMICS-4 and the observation is given in panels a and b. Yellow-shaded regions indicate approximate time intervals when satellite may exit the magnetosphere. Grey-shaded regions show the part of the ICME event simulated also using 0.25 $\mathrm{R_E}$ maximum spatial resolution. Standard deviations (SD) for observation vs. GUMICS-4 (0.5 $\mathrm{R_E}$ resolution) datasets are given in panels a and b.

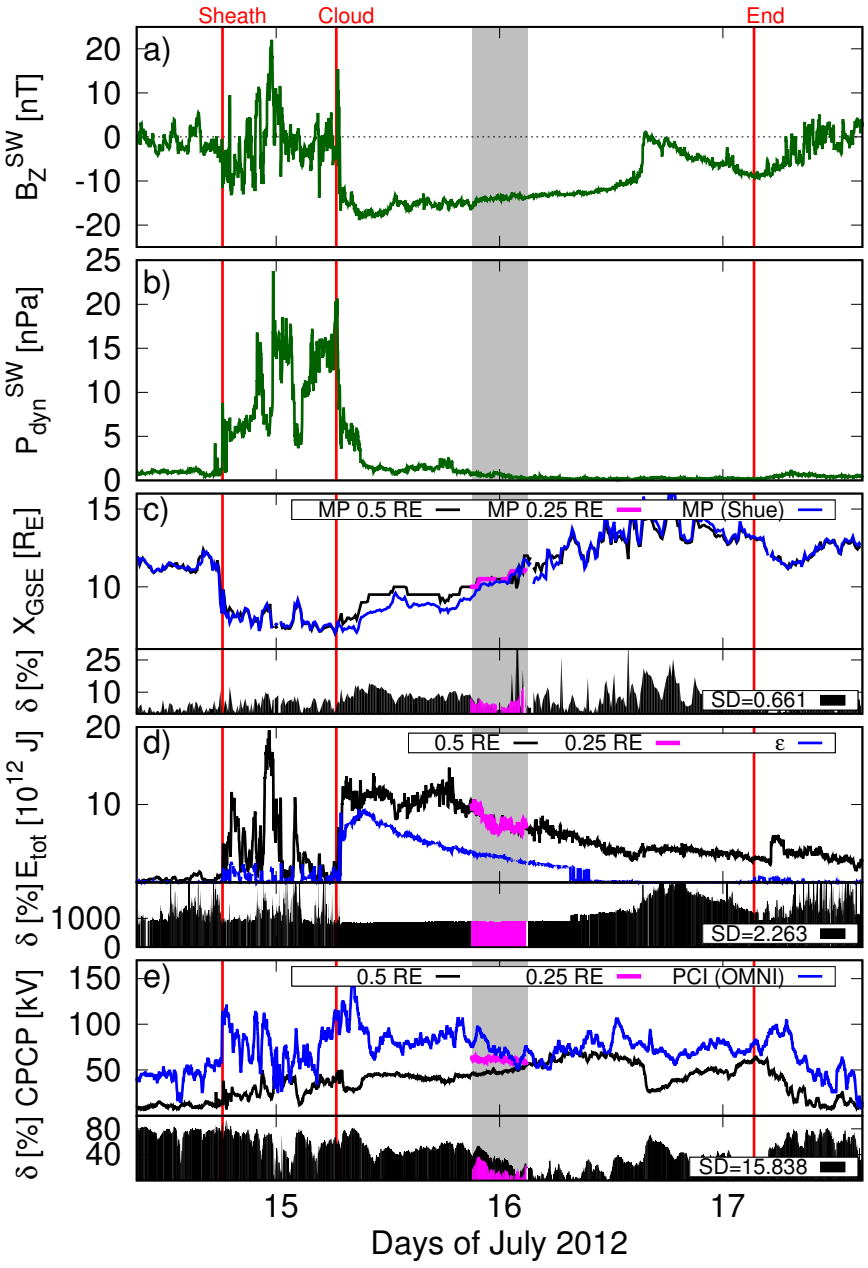

Figure 6. a) Interplanetary magnetic field Z-component, b) solar wind dynamic pressure, c) distance to the nose of the magnetopause, d) energy transferred from the solar wind into the magnetosphere through the dayside magnetopause, and e) the cross-polar cap potential during July 15 21:00 UT - July 16 03:00 UT, 2012. Magenta plots in panels c–d show results with maximum spatial resolution of 0.25 R_E. Blue curves in panels c, d, and e show the reference values (the Shue model, the ϵ-parameter, the PCI index). The relative difference magnitude δ between GUMICS-4 and the reference value is shown in panels c–e. Standard deviations (SD) for reference vs. GUMICS-4 (0.5 R_E resolution) datasets are given in panels c–e.

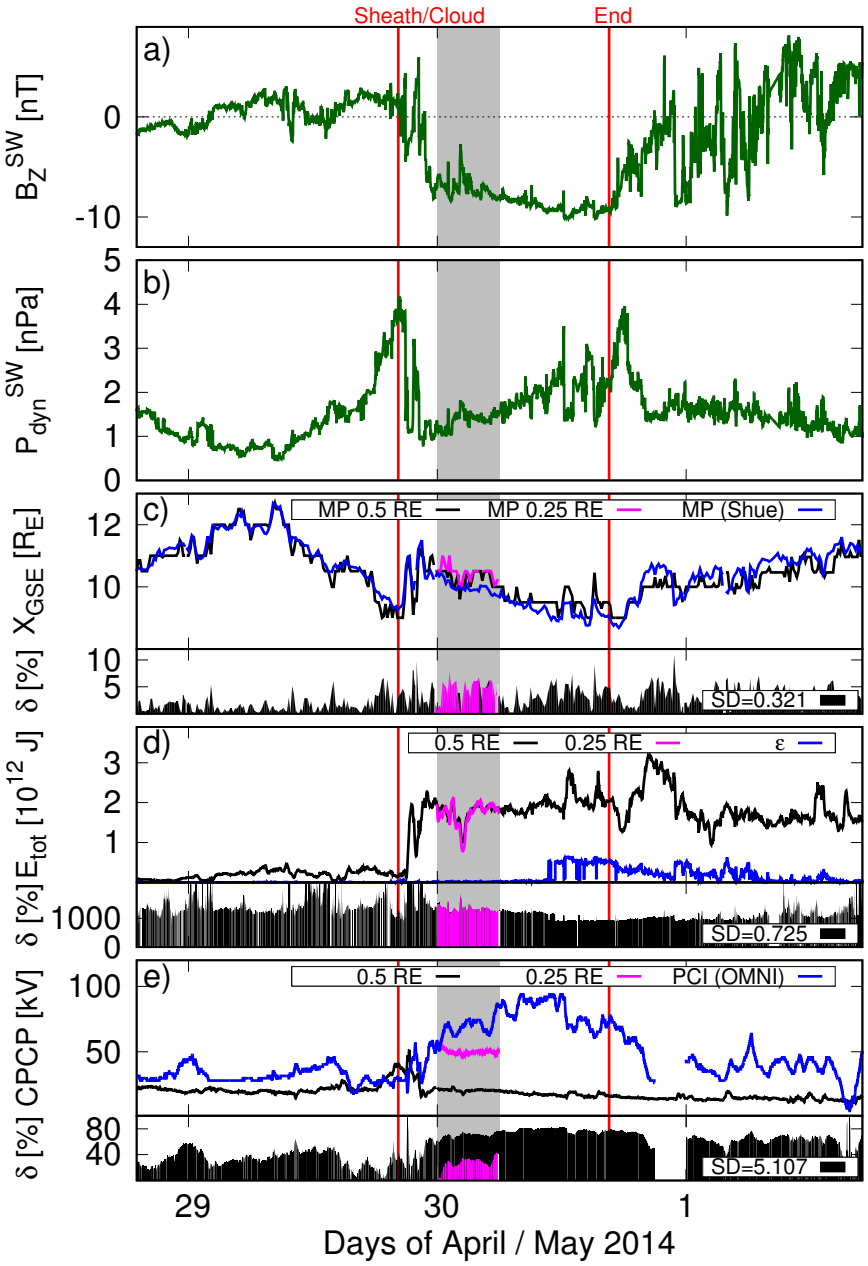

Figure 7. a) Interplanetary magnetic field Z-component, b) solar wind dynamic pressure, c) distance to the nose of the magnetopause, d) energy transferred from the solar wind into the magnetosphere through the dayside magnetopause, and e) the cross-polar cap potential during April 30 00:00 UT – 06:00 UT, 2014. Magenta plots in panels c–d show results with maximum spatial resolution of 0.25 R_E. Blue curves in panels c, d, and e show the reference values (the Shue model, the ϵ-parameter, the PCI index). The relative difference magnitude δ between GUMICS-4 and the reference value is shown in panels c–e. Standard deviations (SD) for reference vs. GUMICS-4 (0.5 R_E resolution) datasets are given in panels c–e.

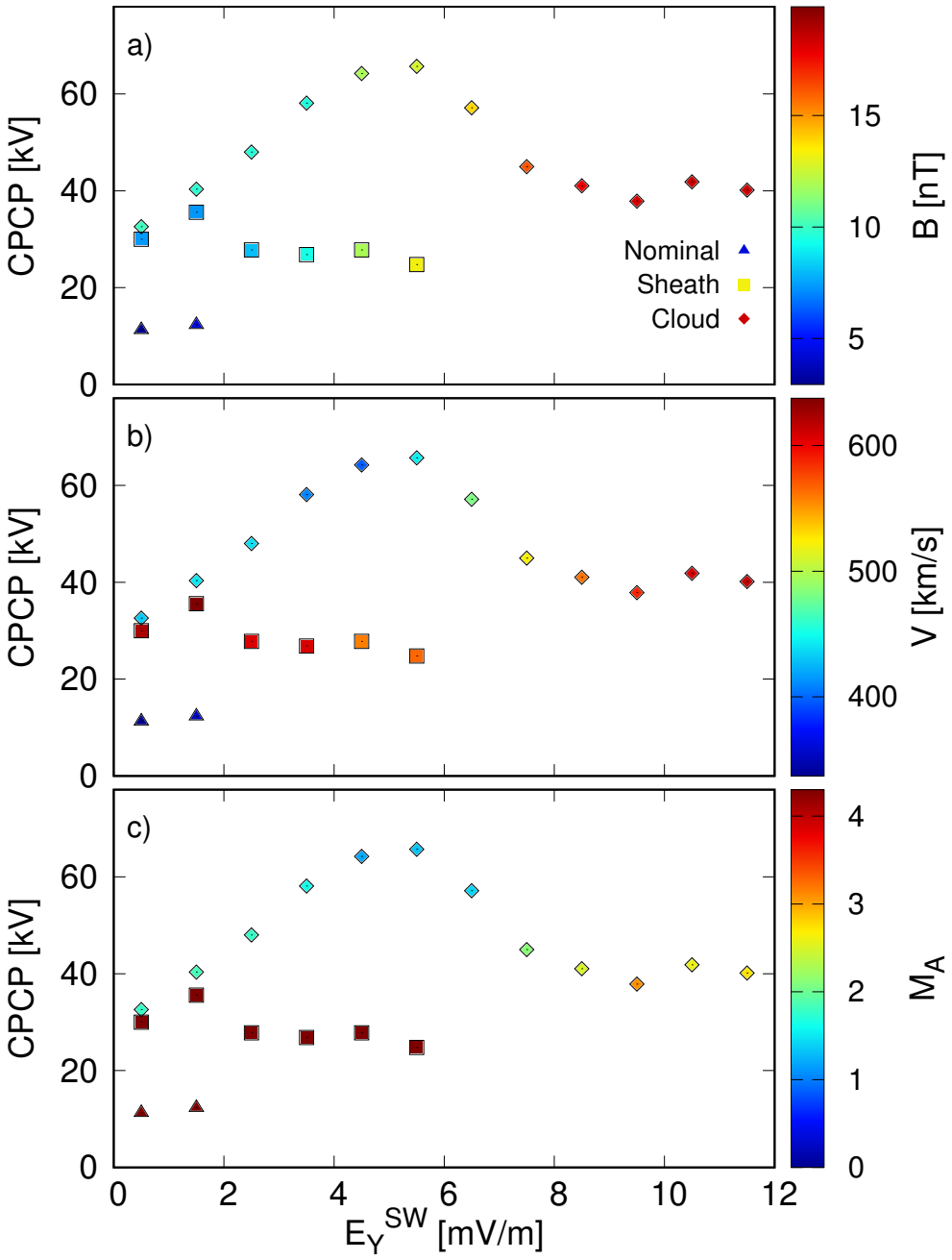

Figure 8. The cross-polar cap potential (CPCP) as a function of the IMF E_Y for the 2012 ICME sheath and cloud periods, with nominal solar wind conditions before and after the ICME event taken into account separately. GUMICS-4 simulation data with 1 minute time resolution has been averaged by 10 minutes and binned by upstream E_Y with 1.0 $\mathrm{mV/m}$ intervals. Panels a, b and c show the magnitudes of the IMF, the upstream flow speed and the Alfvén Mach number, respectively.

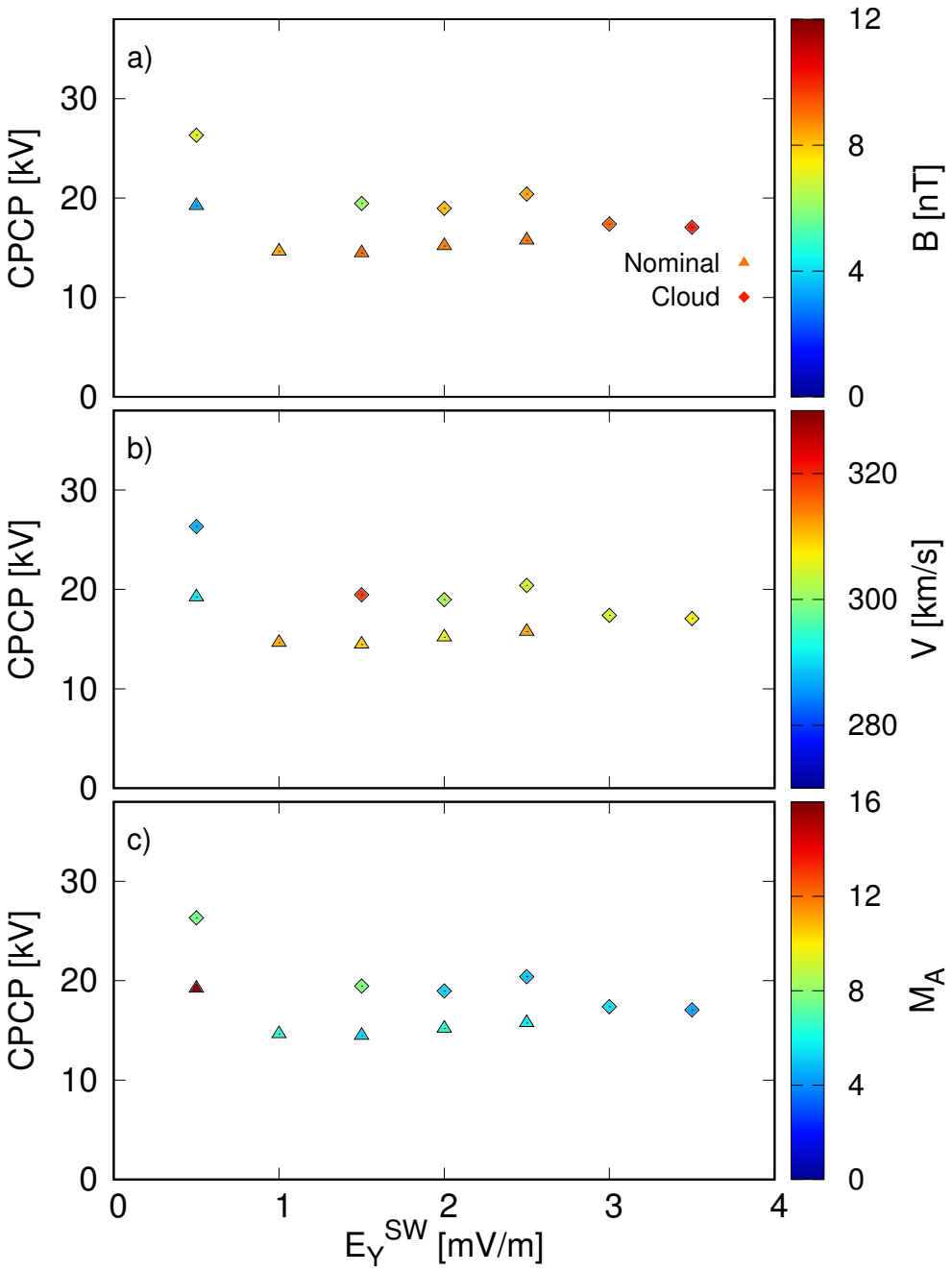

Figure 9. The cross-polar cap potential (CPCP) as a function of the IMF E_Y for the 2014 ICME cloud period, with nominal solar wind conditions before and after the ICME event taken into account separately. GUMICS-4 simulation data with 1 minute time resolution has been averaged by 10 minutes and binned by upstream E_Y with 0.5 $\mathrm{mV/m}$ intervals. Panels a, b and c show the magnitudes of the IMF, the upstream flow speed and the Alfvén Mach number, respectively.

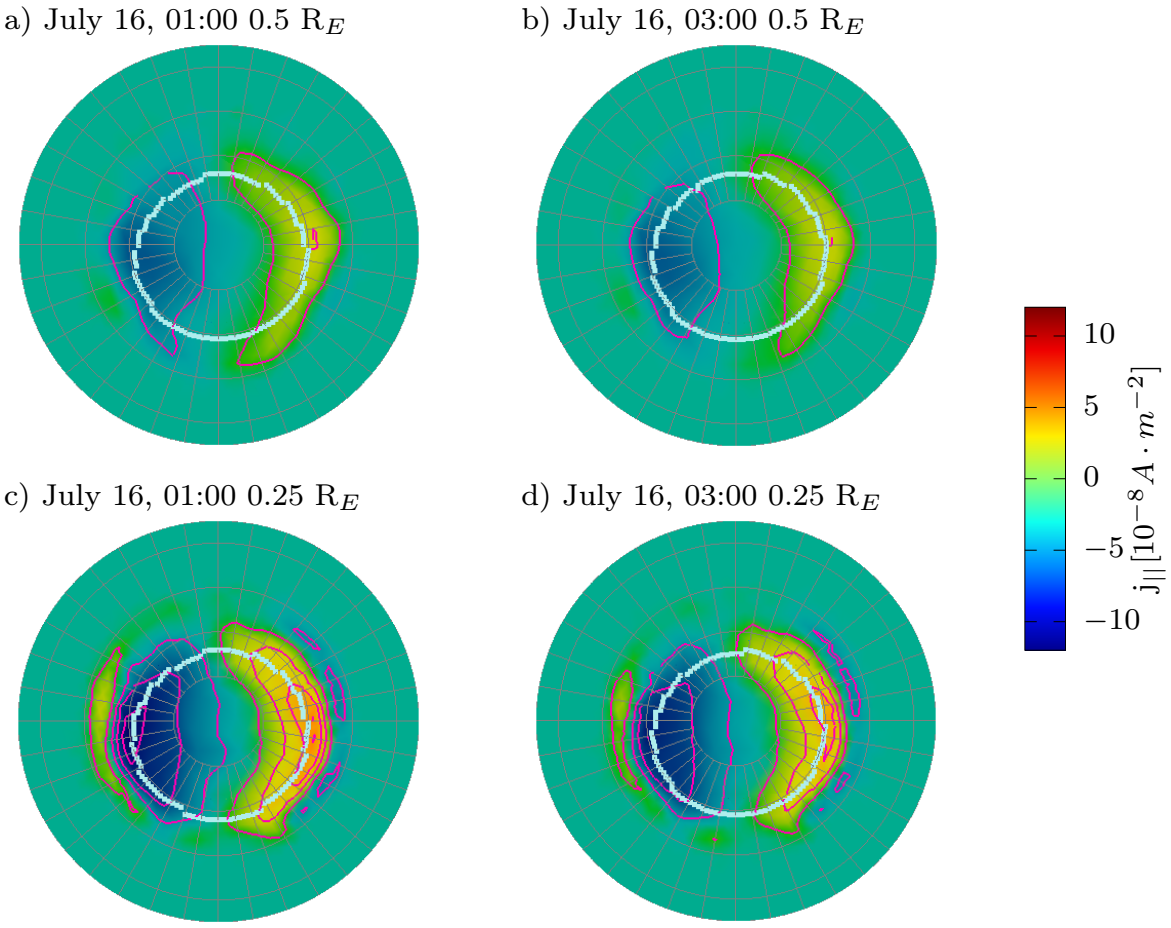

Figure 10. The northern hemisphere field-aligned current pattern in GUMICS-4 simulation at 01:00 UT (panels a and c) and at 03:00 UT (panels b and d) in July 16, 2012. Panels a and b (c and d) show the results of the simulation run in which 0.5 (0.25) R_E maximum spatial resolution was used.